https://doi.org/10.5194/egusphere-2026-2341
Preprint. Discussion started: 2 July 2026

Evaluation of MARv3.14 over the Greenland Ice Sheet

Guillaume Timmermans[1], Brice Noël[1], Christoph Kittel[1,2], Thomas Dethinne[1,3], Nicolas Ghilain[1,4], and Xavier Fettweis[1]

[1]Laboratory of Climatology, Department of Geography, SPHERES research unit, University of Liège, Liège, Belgium
[2]Physical Geography research group, Department of Geography, Vrije Universiteit Brussel, Brussels, Belgium
[3]Geospatial Data Science and City Information Modeling, Department of Geography, SPHERES research unit, University of Liège, Liège, Belgium
[4]Royal Meteorological Institute of Belgium, Uccle, Belgium

Correspondence: Guillaume Timmermans (gtimmermans@uliege.be)

Abstract.

Accurately estimating the surface mass balance (SMB) of the Greenland Ice Sheet (GrIS) is essential to quantify its contribution to sea-level rise. The polar regional atmospheric climate model MAR is widely used to simulate GrIS SMB and to force ice sheet dynamics models, highlighting the need for a thorough evaluation. Here, we evaluate the latest MAR version (MARv3.14) over Greenland at 5 km spatial resolution and examine the impact of coarser resolutions (10–30 km) on the simulated SMB and its components. MAR outputs are compared to a range of independent observations, including in situ SMB measurements, automatic weather station (AWS) records of near-surface meteorological variables, satellite-derived melt extent, and albedo products. At 5 km, MAR reproduces the observed SMB with a root-mean-square error (RMSE) of 0.51 m and a correlation of 0.93. For near-surface meteorological variables and surface energy budget fluxes, the model RMSE is smaller than the corresponding observed natural variability (i.e., standard deviation), indicating non-significant model error. Prescribing bare-ice albedo improves the model performance in the ablation zone, while biases remain in the accumulation zone, suggesting that further improvements are required in the snow albedo scheme. In addition, simulated melt timing is consistent with satellite-based melt extent products. Sensitivity experiments reveal that discrepancies between simulations at different spatial resolutions are mostly limited to the ice sheet margins where strong SMB and topographic gradients occur, notably in the southeast of Greenland where precipitation peaks. Differences in integrated SMB generally remain small and mostly non-significant, while individual components, i.e., precipitation and runoff, exhibit larger resolution-dependent variations. We find that a resolution of at least 10 km is required to accurately capture the GrIS climate and SMB. Reducing computation time about 10-fold relative to 5 km simulation, a 10 km grid makes a good compromise for long-term climate projections.

https://doi.org/10.5194/egusphere-2026-2341
Preprint. Discussion started: 2 July 2026

1 Introduction

The Greenland Ice Sheet (GrIS) has been rapidly losing mass over the last two decades (IMBIE, 2020; Otosaka et al., 2023), and its complete melt would raise sea level by about 7.42 m (Morlighem et al., 2017). This mass loss is driven by a combination of increased solid ice discharge from calving icebergs (Mankoff et al., 2020) and declining Surface Mass Balance (SMB), i.e., the difference between total precipitation (PR ; the sum of snowfall and rainfall), surface runoff (RU), net sublimation (SU) and net drifting snow erosion (ER) (Lenaerts et al., 2019). Overall, solid ice discharge and SMB contribute roughly equally to the observed mass loss (IMBIE, 2020). In the future, mass loss from dynamic processes may decrease as glaciers retreat, potentially enhancing the relative contribution of surface processes (Goelzer et al., 2013; Enderlin et al., 2014; Fürst et al., 2015). However, recent work highlights substantial uncertainties, and some evidence suggests that ocean-driven calving could continue to play a significant role in future mass loss (Choi et al., 2021).

Several approaches have been developed to estimate the GrIS SMB including positive degree days, energy balance, regional (RCM) or global circulation models (GCM) (Fettweis et al., 2020). In particular, the *Modèle Atmosphérique Régional* (MAR) (Gallée and Schayes, 1994) is a key tool to reconstruct the present climate (Fettweis, 2007; Fettweis et al., 2017) and further project GrIS SMB under future atmospheric warming (Fettweis et al., 2013; Glaude et al., 2024).

Similarly to other RCMs (see e.g. Box and Rinke, 2003; Langen et al., 2017; Niwano et al., 2018; Noël et al., 2018), previous MAR versions (e.g. 3.9) have been evaluated over the GrIS (e.g. Delhasse et al., 2020; Fettweis et al., 2020). Since then, numerous developments have been implemented in versions 3.10–3.14, as well as an increase in spatial resolution over the Greenland domain, i.e., from 15 km (Fettweis et al., 2020) to 5 km in this study.

Here, we assess the GrIS climate and SMB simulated by the latest version of MAR (3.14) using a comprehensive suite of observational products, including in situ SMB measurements, meteorological and surface energy budget (SEB) variables measured at automatic weather stations (AWS), remotely sensed melt extent, and albedo. This constitutes the most exhaustive MAR evaluation to date since previous studies typically focused on a single component of the system, e.g., SMB (Fettweis et al., 2020), AWS-based variables (Delhasse et al., 2020), albedo (Antwerpen et al., 2022; Ernotte, 2025), or melt extent (Fettweis et al., 2005). We aim to provide a comprehensive overview of model performance, offering physical insights into the drivers of simulated SMB biases. Here simulations are conducted at 5 km horizontal resolution and forced by ERA5 reanalysis on a 6-hourly basis over the 1979–2024 period.

To date, MAR has often been used at spatial resolutions coarser than 5 km. For example, the Ice Sheet Model Intercomparison Project for CMIP6 (ISMIP6; Goelzer et al., 2020) used MARv3.12 outputs at 15 km resolution, while Delhasse et al. (2024) ran MARv3.11.5 at 25 km resolution. Moreover, long term projections were conducted using MAR at 25–30 km resolution in e.g., Franco et al. (2013) and Paice et al. (2025) (MARv3.13). As SMB products differ across resolutions (Franco et al., 2012), we therefore explore the impact of spatial resolution on GrIS SMB representation by comparing MARv3.14 simulations at 5, 10, 15, 20, and 30 km resolution, enabling us to determine the minimum resolution required to realistically capture GrIS surface processes.

https://doi.org/10.5194/egusphere-2026-2341
Preprint. Discussion started: 2 July 2026

In Section 2, we first describe MARv3.14, the latest model developments, and our experimental setup. We then present the observational datasets used for model evaluation (in situ SMB, near-surface meteorology, albedo, and melt extent). In Section 3, we evaluate GrIS climate and SMB as modelled by MAR at 5 km and examine the impact of spatial resolution on modelled GrIS SMB. The evaluation of MAR at 5 km follows a diagnostic progression, starting with the integrated SMB to establish the overall model state, before investigating the underlying meteorological, radiative, and albedo-driven causes of simulated biases. We discuss and link our results in Section 4, and draw conclusions in Section 5.

2 Model and observational data

2.1 Regional climate model MARv3.14

MAR is a regional climate model (Gallée and Schayes, 1994) coupled to the one-dimensional Snow, Ice, Soil, Vegetation, Atmosphere Transfer (SISVAT) surface scheme (De Ridder and Gallée, 1998). It has been specifically adapted to simulate the climate and SMB of polar ice sheets and glaciers, including those of Greenland (Delhasse et al., 2020), Antarctica (Kittel et al., 2018, 2021), the Arctic region (Lang et al., 2015; Maure et al., 2023), and Patagonia (Noël et al., 2025). Recent developments have extended MAR domains to mid-latitude regions such as Belgium (Wyard et al., 2017; Doutreloup et al., 2019; Grailet et al., 2025; Brajkovic et al., 2025), the Black Sea (Macé et al., 2025), and the Vosges mountains (Fettweis et al., 2023).

Previous MAR versions were described in Amory et al. (2021) and in Kittel et al. (2021) (MARv3.11), Antwerpen et al. (2022) (MARv3.12), or in Fettweis et al. (2023) (MARv3.13). Compared to the latter versions, MARv3.14 implements the ECMWF radiative scheme (Hogan and Bozzo, 2018), as detailed in Grailet et al. (2025). Additional modifications include enforcement of water conservation within the soil and snowpack; an updated parameterization of maximum liquid water content (7 % at the snow surface, decreasing linearly to 2 % at 1 m depth); and a continuous snowfall-to-rainfall transition between -1°C (100 % snow) and 1 °C (100 % rain) for precipitation generated by the turbulence and convective schemes (Haacker et al., 2024). For the Greenland domain, MARv3.14 prescribes bare-ice albedo (BIA) using MODIS observations (Schaaf and Wang, 2015), instead of a surface meltwater dependent bare ice albedo ranging between 0.5 and 0.55 (Antwerpen et al., 2022) used in previous versions. BIA is derived from a 15-days-averaged MODIS albedo product as the annual 5 % lowest measured albedo averaged for the period 2000–2023, following Noël et al. (2018). This low-end quantile is assumed to capture snow-free bare-ice conditions. MARv3.14 also allows surface meltwater to refreeze above bare ice (Timmermans, 2024).

Here, MAR is forced at its lateral and upper (in the stratosphere) boundaries by the ERA5 reanalysis (Hersbach et al., 2020) on a six-hourly basis. Atmospheric forcing includes temperature, specific humidity, wind components, and pressure at each vertical model level. A relaxation zone is applied at the lateral boundaries to nudge the model variables towards the boundary conditions. In addition to atmospheric forcing, sea surface temperature and sea ice extent are prescribed on a six-hourly basis from ERA5 reanalysis.

The ice sheet grid-cell fraction is prescribed from the PROMICE mask (Luetzenburg et al., 2025). The surface topography is down-sampled from the ArcticDEM at 90 m spatial resolution (Porter et al., 2022) onto the 5 km grid.

https://doi.org/10.5194/egusphere-2026-2341
Preprint. Discussion started: 2 July 2026

2.2 Comparing MAR at different resolutions

To explore the sensitivity of MAR to spatial resolution, we conduct and compare simulations at 5, 10, 15, 20 and 30 km over the 1979–2024 period. Contiguous GrIS SMB (and its components) are spatially integrated over MAR native grids at each resolution. Peripheral glaciers and ice caps are excluded from the analysis. Since MAR implements grid-cell fractionation, each grid-cell is weighted by its ice fraction when computing spatially integrated SMB. Grid-cells with an ice fraction lower than 50 % are discarded to avoid unrealistically high ablation values near the ice sheet–tundra interface.

2.3 In situ SMB data

We use SMB measurements from the GrIS SUMup database (Vandecrux et al. (2024) ; purple dots in Figure 1a). Here, we compare modelled SMB with measurements derived from stakes, snow pits, firn and ice cores, snowfox records, mass balance profile estimates and δ^{18}O dating. In addition, we complement the SUMup dataset with ice-core measurements from the GrIS accumulation zone (Ohmura and Reeh (1991) ; green squares in Figure 1a). In Section 4, we also use the in situ SMB measured by pressure transducers at PROMICE stations (Vandecrux et al., 2024). The temporal resolution of SMB (or accumulation rate) measurements varies depending on the method, ranging from sub-daily records (e.g., pressure transducers) to seasonal or multi-annual estimates derived from stake measurements, snow pits, and ice cores.

To evaluate the SMB simulated by MAR, we follow the general protocol of Fettweis et al. (2020). For each in situ SMB observation, a corresponding MAR value is obtained applying an inverse distance weighting (IDW) interpolation using the four nearest model grid-cells (as explained in Appendix A). Modelled SMB is then integrated over the period overlapping observations, in line with Fettweis et al. (2020). In contrast to Fettweis et al. (2020), we do not apply an elevation correction unless explicitly stated. When applied, topographic correction ($\mathrm{SMB_{corr}}$) is computed as follows (Eq. (1)):

$$\mathrm{SMB_{corr}} = \mathrm{SMB_{IDW}} + \beta\,\Delta z, \qquad \Delta z = z_{\mathrm{obs}} - z_{\mathrm{IDW}}, \tag{1}$$

where $\mathrm{SMB_{IDW}}$ is the IDW-interpolated SMB, β is the local (i.e., based on the four closest pixels) SMB–elevation regression slope, z_{obs} the altitude of the observation, and z_{IDW} the IDW-interpolated elevation.

2.4 Automatic weather stations data

We compare daily modelled meteorological variables and SEB fluxes with observations from 51 AWS compiled in the PROMICE and GC-NET datasets (Fausto et al., 2021; How et al., 2022; Vandecrux et al., 2023) (black crosses with yellow contour in Figure 1a). Meteorological variables include near surface temperature, specific humidity, wind speed, and surface pressure. In the observational datasets, SEB components include downward and upward shortwave and longwave radiation, whereas sensible and latent heat fluxes are not measured but rather inferred from other recorded variables. Therefore, we only compare MAR to observed SEB radiative fluxes. The full observational data set spans 1990–2024, though the temporal coverage differs

https://doi.org/10.5194/egusphere-2026-2341
Preprint. Discussion started: 2 July 2026

among stations. AWS measurements are recorded at 10-minute intervals that are averaged daily for a consistent comparison with MAR daily outputs.

For SEB, we identified and removed outliers in the AWS dataset by excluding unrealistically high shortwave fluxes ($>$ 450 $\mathrm{W\,m^{-2}}$), likely caused by erratic surface reflection over ice. We discarded upward longwave fluxes exceeding the theoretical blackbody limit of $\sim$ 315.7 $\mathrm{W\,m^{-2}}$ (i.e., σT^4, where $T = 273.15$ K and $\sigma = 5.67$ $\mathrm{W\,m^{-2}\,T^{-4}}$, namely the Stefan–Boltzmann constant). This is consistent with other RCM evaluations (see e.g., Noël et al., 2018).

We adopt the same comparison approach as that described for SMB (Section 2.3). Each daily observation is paired with the IDW-interpolated MAR value without topographic correction.

2.5 Satellite albedo data

We compare MAR-modelled albedo with broadband snow albedo derived from the Ocean and Land Colour Instrument (OLCI) operating on Sentinel-3 by the Geological Survey of Denmark and Greenland (GEUS) (Vandecrux et al., 2021). The comparison period spans 2017 to 2019, inclusive. We restrict our analysis to the months of May through October, since wintertime albedo retrievals are neither available nor particularly relevant at high latitudes due to limited solar radiation. The OLCI-GEUS product is provided at a native resolution of 1 km and at a daily time interval. To enable a consistent comparison with MAR, we aggregate the OLCI-GEUS data by averaging all 1 km pixels whose centres fall within a same MAR grid-cell.

We also compare MAR-modelled albedo to broadband in situ surface albedo measured at PROMICE and GC-NET AWSs (How et al., 2022; Fausto et al., 2021; Vandecrux et al., 2023). To do so, we pair station measurements with the corresponding IDW-interpolated MAR values for their overlapping periods.

2.6 Melt extent satellite data

Passive microwave satellite sensors provide information on the snowpack wetness (see e.g., Torinesi et al., 2003; Picard et al., 2022). Since the snowpack is wet during melt episodes, these observations are often referred to as melt extent measurements (e.g., Fettweis et al., 2011), though the term wet snow mask (Dethinne et al., 2023; Leduc-Leballeur et al., 2026) better reflects the recorded signal. Here we use the product of Picard (2025), that combines melt extent maps derived from the Advanced Microwave Scanning Radiometer E (AMSR-E, 2002–2011) and 2 (AMSR2, 2012–present) observations provided by the Japan Aerospace Exploration Agency (JAXA). The dataset consists of daily binary melt masks (1 for melt detected, 0 for no melt) at a spatial resolution of 10 km over the GrIS, separately for ascending and descending satellite overpasses, using the third band at 18.7 GHz. Data are sampled daily.

We combine the ascending and descending overpasses by applying a logical "OR" operation, to estimate the maximum daily melt extent. These melt extent data are further corrected using the first two steps of the filtering algorithm described in Fettweis et al. (2006), which ensures the continuity of the melt season (step 1) and extends melt detection to pixels surrounded by at least three adjacent higher-altitude ones experiencing melt (step 2).

To compare MAR outputs with satellite observations, a criterion must be applied to convert the model variables into a binary indicator of melt (melt / no melt, or wet / dry). We present and discuss the results obtained using a melt rate–based criterion,

https://doi.org/10.5194/egusphere-2026-2341
Preprint. Discussion started: 2 July 2026

whereby a grid-cell is classified as melting when the simulated melt exceeds a threshold of 0.2 $\mathrm{mm\,w.e.\,day^{-1}}$, following Fettweis et al. (2011) and Puggaard et al. (2025).

The comparison is performed over the 2002–2024 period, after interpolating MAR data onto the satellite data grid at 10 km using the IDW approach.

3 Results

3.1 SMB modelling

We compare MAR-simulated SMB at 5 km to in situ SMB measurements from Vandecrux et al. (2024), and Ohmura and Reeh (1991), following the same approach as Fettweis et al. (2020) (Fig. 1).

At 5 km, MAR shows a SMB bias of 0.11 $\mathrm{m\,w.e.}$, a RMSE of 0.51 $\mathrm{m\,w.e.}$, and a correlation of 0.93 (Fig. 1b). Applying topographic correction (Eq. (1)), SMB bias and RMSE decrease by 27 % and 20 % respectively, while correlation increases to 0.95 (Fig. 1c). The linear regression lines, which exhibit slopes lower than 1, indicate that MAR tends to underestimate both high ablation and high accumulation observed values. In particular, for SMB observations lower than -5 $\mathrm{m\,w.e.}$, MAR systematically underestimates the ablation. As a comparison, the mean and the standard deviation of the in situ SMB observations are -0.56 and 1.29 $\mathrm{m\,w.e.}$, respectively. To assess error significance, we compare the modelled RMSE with the observed standard deviation of the corresponding variables, i.e., representative of the observed natural variability. Here, model SMB error is non-significant, with modelled RMSE (0.51 $\mathrm{m\,w.e.}$) being 60 % smaller than the observed standard deviation (1.29 $\mathrm{m\,w.e.}$).

For accumulation evaluation, we compare MAR SMB outputs to ice cores from Ohmura and Reeh (1991) (green squares in Figure 1a), yielding good agreement with high correlation (0.92) and non-significant RMSE (0.08 $\mathrm{m\,w.e.}$), i.e., half the observed standard deviation (0.16 $\mathrm{m\,w.e.}$). Unfortunately, due to the extreme weather conditions, no (in situ) measurement is available in southeast Greenland where modelled accumulation peaks, as mentioned by Fettweis et al. (2020), preventing thorough model evaluation.

In addition, we evaluated MAR SMB under the exact same conditions (over 1980–2012) as in the GrISSMBMIP intercomparison of Fettweis et al. (2020) (Table S1). We find that MARv3.14 (5 km) improves on MARv3.9 (15 km), while model differences remain statistically non-significant. Comparing MARv3.14 to airbone radar transects from Karlsson et al. (2016, 2020) leads to biases, RMSEs and correlations of -0.01 $\mathrm{m\,w.e.}$ and 0.02 $\mathrm{m\,w.e.}$ and 0.99, similar to those of MARv3.9. This demonstrates the robustness of the model irrespective of the selected version.

At lower spatial resolution (10–30 km), biases and RMSEs increase (from 0.22 and 0.70 $\mathrm{m\,w.e.}$, respectively at 10 km to 0.36 and 0.98 $\mathrm{m\,w.e.}$ at 30 km) while correlations decrease (from 0.87 at 10 km to 0.72 at 30 km). However, we note that RMSE remains lower than the standard deviation of the SMB observations (i.e., 1.29 $\mathrm{m\,w.e.}$) even at 30 km spatial resolution (0.98 $\mathrm{m\,w.e.}$, roughly twice the 5 km RMSE), indicating overall non-significant model errors. Detailed statistics for different spatial resolutions spanning 10–30 km are listed in Table S2.

https://doi.org/10.5194/egusphere-2026-2341
Preprint. Discussion started: 2 July 2026

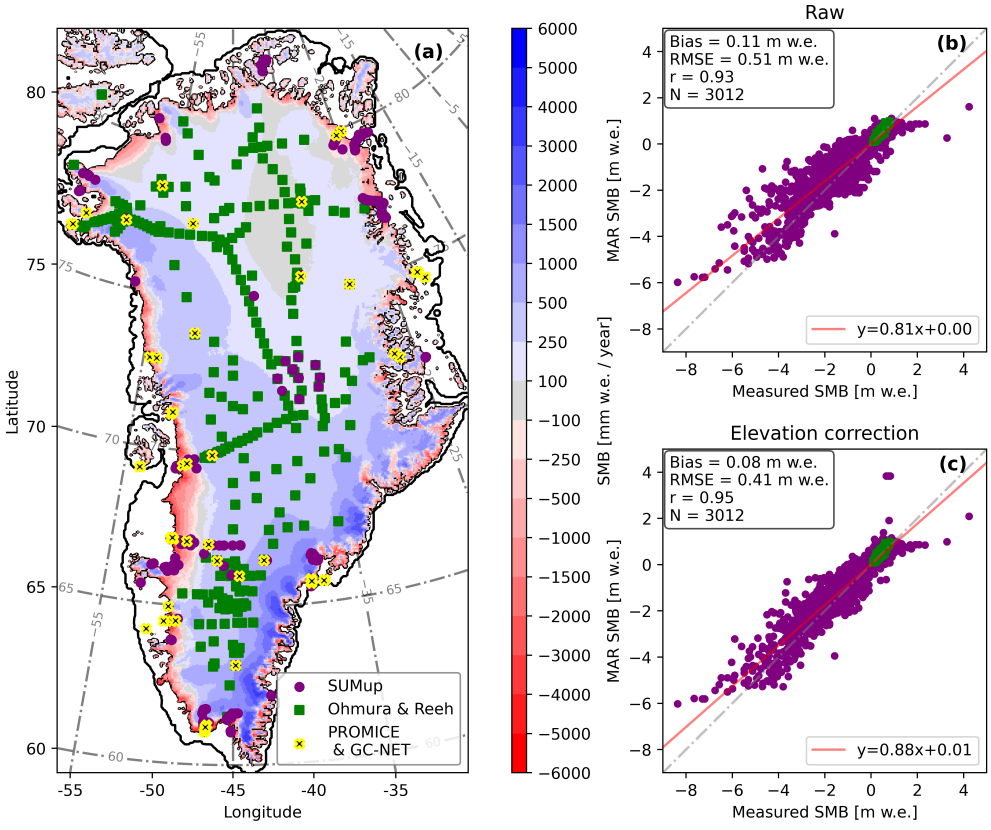

Figure 1. (a) Mean annual surface mass balance (SMB) as modelled by MARv3.14 at 5 km resolution averaged for the period 1979–2024 (in metres water equivalent, m w.e.). Black lines delineate continental coastlines. Note that the color scale is non-linear. Station location used for SMB evaluation are also shown, including SUMup (Vandecrux et al. (2024); purple dots), Ohmura and Reeh (1991) (green squares) and PROMICE & GC-NET (Fausto et al., 2021; How et al., 2022; Vandecrux et al., 2023) (black crosses with yellow contour) automatic weather stations. Scatterplots comparing (b) raw modelled SMB using IDW and (c) elevation corrected SMB with the observational datasets (see Eq. (1)). Statistics include: number of observations (N), correlation (r), mean bias, and Root Mean Square Error (RMSE). Least squares linear regression lines are shown in red.

https://doi.org/10.5194/egusphere-2026-2341
Preprint. Discussion started: 2 July 2026

3.2 Near-surface meteorology

To evaluate the representation of near-surface meteorological variables in MAR, we compare modelled near-surface temperature, specific humidity, wind speed, and surface pressure with AWS observations from the PROMICE and GC-NET networks (Fausto et al., 2021; How et al., 2022; Vandecrux et al., 2023). The results are shown in Figure 2a–d.

MAR at 5 km reproduces near-surface temperature, specific humidity, and pressure with high correlations ($0.97 < r < 0.99$) and small biases (resp. RMSE) of 0.21 °C, 0.05 $\mathrm{g\,kg^{-1}}$, and -3.10 hPa (resp. 2.49 °C, 0.36 $\mathrm{g\,kg^{-1}}$ and 15.41 hPa). Wind speed shows a lower correlation (0.78), with a bias of -0.13 $\mathrm{m\,s^{-1}}$ and an RMSE of 1.98 $\mathrm{m\,s^{-1}}$. Strong winds (> 5 $\mathrm{m\,s^{-1}}$) are generally underestimated (Fig. 2c). Regarding surface pressure, the atypical shape of the scatterplot (Fig. 2d) arises from elevation differences between the stations and the nearest MAR grid-cells. Applying a topographic correction to the pressure comparison removes this pattern and reduces both the bias and RMSE of surface pressure by roughly a factor of 3. The observed annual (resp. summer, i.e., June–July–August or JJA) standard deviations of meteorological variables are 11.1 °C (resp. 5.08 °C) for near-surface temperature, 1.36 $\mathrm{g\,kg^{-1}}$ (resp. 1.02 $\mathrm{g\,kg^{-1}}$) for specific humidity, 3.10 $\mathrm{m\,s^{-1}}$ (resp. 2.44 $\mathrm{m\,s^{-1}}$) for wind speed, and 89.22 hPa (resp. 87.69 hPa) for surface pressure. The latter are larger than the corresponding MAR-modelled RMSEs, indicating that these are not significant (i.e., lower than the natural variability).

At coarser resolutions (Table S3), the agreement with observations decreases slightly in terms of RMSE, correlation and bias. However, the differences are small, and the RMSEs remain systematically lower than the corresponding standard deviations.

3.3 Radiative fluxes modelling

A similar comparison is performed for SEB radiative fluxes, i.e., downward/upward shortwave (SWD/SWU) and longwave radiation (LWD/LWU), in Figure 3a–d. Except for the RMSEs which are slightly larger for shortwave fluxes ($\sim$ 12 $\mathrm{W\,m^{-2}}$), no significant differences are found between the annual and the summer (JJA) statistics (Table S4). The correlations range from 0.89 to 0.96. Negative biases indicate a general underestimation of radiative fluxes in MAR, notably for large fluxes, as shown by the slope of the regression lines in Figure 3 (i.e., lower than 1). The (absolute) biases range from 0.65 $\mathrm{W\,m^{-2}}$ for LWU to 1.78 $\mathrm{W\,m^{-2}}$ for SWU, except for LWD (-9.78 $\mathrm{W\,m^{-2}}$). RMSE values range from 11 to 35 $\mathrm{W\,m^{-2}}$, and are overall lower than the observed variability. The annual (resp. JJA) standard deviations (in $\mathrm{W\,m^{-2}}$) are 129.95 (resp. 93.60) for SWD, 50.08 (resp. 35.98) for LWD, 99.01 (resp. 91.84) for SWU, and 38.98 (resp. 18.85) for LWU.

At lower spatial resolutions (Table S4), in line with SMB (and near-surface meteorological variables), model performance decreases, but the model RMSEs remain below the standard deviation of the observations irrespective of the spatial resolution.

Similarly, Delhasse et al. (2020) showed that MARv3.9 simulates downward shortwave and longwave radiative fluxes less accurately than reanalyses, which was attributed to the absence of satellite data assimilation and the use of an outdated radiative scheme. Since MARv3.14 includes an updated radiative scheme (Grailet et al., 2025), we repeated the AWS comparison under identical conditions. The results are presented in Table S5 and show only marginal improvement relative to MARv3.9. This suggests that the remaining biases are not solely related to the radiative scheme itself, but may also arise from an inaccurate representation of clouds (both liquid and solid), which remains a major challenge in atmospheric modelling (Fridlind et al.,

https://doi.org/10.5194/egusphere-2026-2341
Preprint. Discussion started: 2 July 2026

2007). Cloud cover strongly modulates both downward shortwave and longwave radiative fluxes (Mostue et al., 2024), contributing to discrepancies with PROMICE observations. A dedicated evaluation of cloud representation in MAR, following the methodology of Wang et al. (2019), would therefore provide valuable guidance for further model development.

Note that our results show similar biases and correlation to those obtained from another RCM (i.e., RACMO2.3p2 at 5 km (Noël et al., 2019) using the same near-surface meteorological variables and radiative fluxes. Both MAR and RACMO2 tend to underestimate high wind speed. The underestimation of peak wind speeds may stem from the model's reliance on a local turbulence scheme, which potentially fails to account for the downward transfer of momentum from higher atmospheric levels by large-scale eddies (Amory et al., 2021).

3.4 Albedo representation

Daily OLCI GEUS albedo values (Vandecrux et al., 2021) were averaged onto the MAR domain to allow a grid-cell by grid-cell comparison, yielding a mean bias of -2×10^{-3}, RMSE of 0.08, and a correlation of 0.70 (Table S6). The same analysis over JJA months led to slightly better results, with a bias of 10^{-4}, RMSE of 0.08 and a correlation of 0.75 (Table S6). Figure 4 shows a spatial comparison of albedo, with coloured points in Figure 4c representing the JJA albedo bias between MAR and the PROMICE & GC-NET AWSs observations.

We find that MAR overestimates albedo along the western and eastern margins of the GrIS by $\sim$ 0.05–0.10, while underestimating it by approximately 0.10 inland and in northwestern areas (Fig. 4c). These opposed regional biases compensate each other when spatially averaged, resulting in a relatively low mean bias of -2×10^{-3} with a larger RMSE (0.08).

Figure 4c shows that the RMSE exceeds the OLCI-GEUS standard deviation over a large fraction of the GrIS (hatched), roughly corresponding to the accumulation zone, where albedo remains nearly constant throughout the year (Fig. 1a). This pattern is partly due to the very low OLCI-GEUS standard deviation in this region, but also reflects a systematic negative bias (~ -0.10), likely originating from the inability of the snow albedo scheme of MAR to capture high fresh snow surface albedo (~ 0.87) in accumulation zones.

The spatial patterns of the MAR–OLCI GEUS differences are broadly consistent with those obtained between MAR and PROMICE & GC-NET measurements (Fig. 4c). In particular, most AWSs located near the southwestern margins generally exhibit a positive albedo bias (except for the two LYN AWSs located at roughly 53.6°W, 69°N), whereas stations in the interior of the GrIS show small biases, typically within $\pm$ 0.025. Figure 5a shows the JJA comparison of albedo between MAR and in situ PROMICE & GC-NET AWSs. We find that MAR overestimates low albedo values in ablation zones exposing bare ice in summer. In fact, MAR does not simulate values below 0.35 whereas values as low as 0.1 are measured by AWSs. This discrepancy stems from the MAR albedo scheme, which constrains the prescribed MODIS-derived ice albedo between 0.35 and 0.55 to prevent the development of unrealistically low albedo values over large areas (25 km^2). In accumulation zones, MAR underestimates snow albedo although with lower bias, RMSE and variability than in ablation zones.

As discussed above, MAR at 5 km tends to underestimate the downwards radiative fluxes (Fig. 3a–b). Along with the albedo underestimation in the ablation zone, this results in an underestimation of the absorbed shortwave radiative energy at the surface ($\mathrm{SWD_{abs}}$). Figure 5b shows the JJA comparison between MAR and PROMICE & GC–NET AWSs for $\mathrm{SWD_{abs}} =$

https://doi.org/10.5194/egusphere-2026-2341
Preprint. Discussion started: 2 July 2026

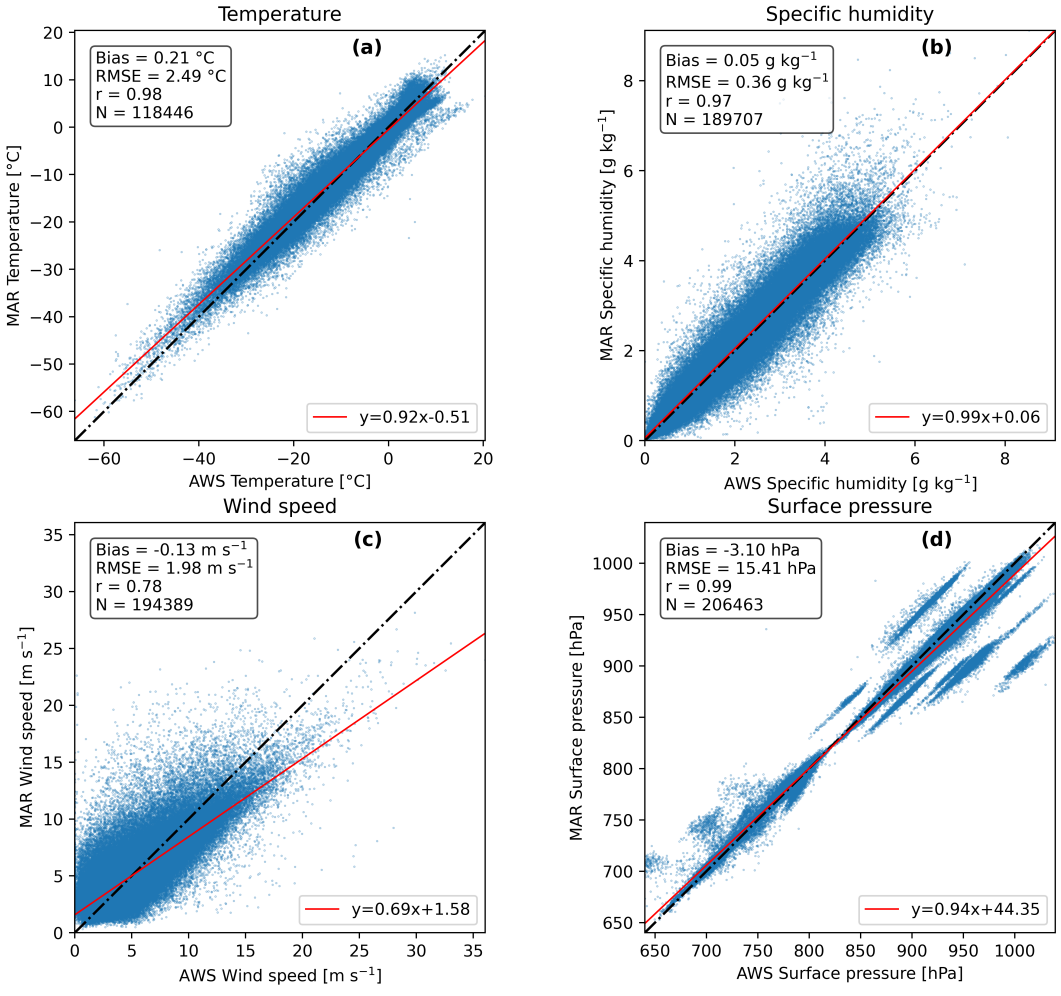

Figure 2. Comparison between MAR-simulated and AWS-observed near-surface meteorological variables, including (a) 2-m air temperature (°C), (b) specific humidity (g kg^{-1}), (c) wind speed (m s^{-1}), and (d) surface pressure (hPa) at 5 km resolution. Each point corresponds to daily mean values interpolated to AWS locations using an inverse distance weighting (IDW) method. No topographic correction is applied. For each scatterplot, associated statistics are shown: means bias, Root Mean Square Error (RMSE), correlation (r) and number of observations (N). The 1:1 lines are shown as black dashed lines. The least squares regression lines are displayed in red.

https://doi.org/10.5194/egusphere-2026-2341
Preprint. Discussion started: 2 July 2026

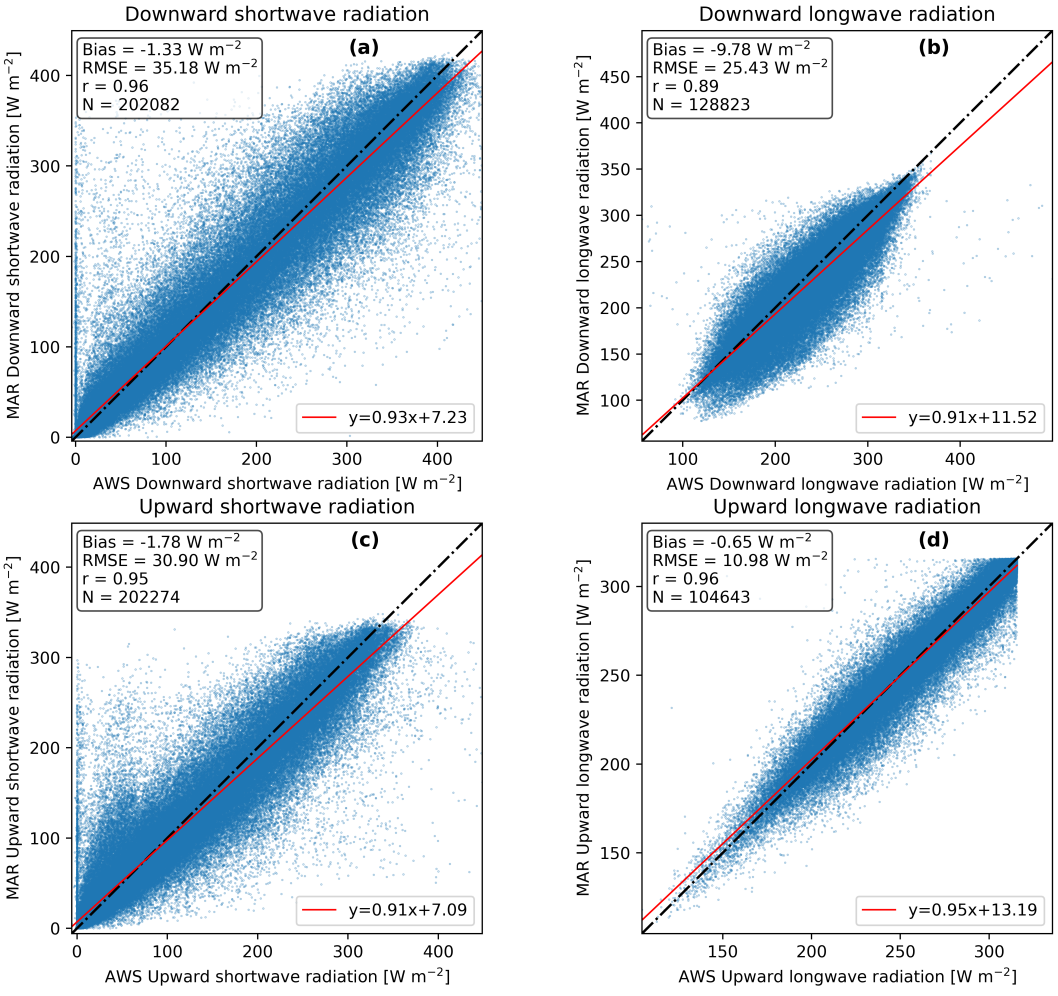

Figure 3. Comparison between radiative surface energy budget (SEB) components (W m^{-2}), including downward (a) shortwave and (b) longwave, upward (c) shortwave and (d) longwave radiation fluxes as simulated by MAR at 5km resolution and measured at PROMICE and GC-NET AWSs. No topographic correction is applied. For each scatterplot, associated statistics are shown: means bias, Root Mean Square Error (RMSE), correlation (r) and number of observations (N). The 1:1 lines are shown as black dashed lines. The least squares regression lines are displayed in red. In (d), we discarded values > 315.7 W m^{-2}, the theoretical blackbody limit, as mentioned in Section 2.4.

https://doi.org/10.5194/egusphere-2026-2341
Preprint. Discussion started: 2 July 2026

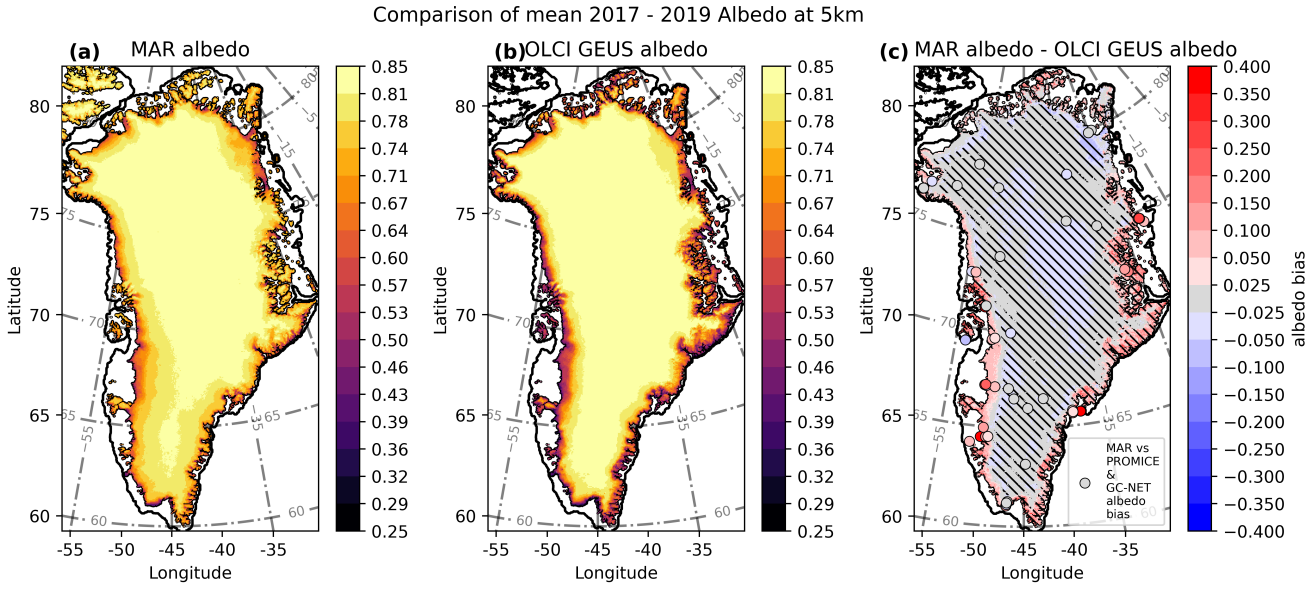

Figure 4. Mean JJA albedo from (a) MAR at 5 km, (b) OLCI GEUS (Vandecrux et al., 2021) averaged onto the MAR 5 km grid, and (c) the MAR–OLCI GEUS difference for 2017–2019. Coloured circles in (c) indicate MAR JJA albedo bias relative to PROMICE and GC-NET AWS observations (How et al., 2022; Fausto et al., 2021; Vandecrux et al., 2023). Diagonal hatching indicates grid points where the RMSE exceeds the local OLCI GEUS standard deviation. Black lines delineate continental coastlines

$(1-\alpha) \times \mathrm{SWD}$, where α is the surface albedo and SWD the downward shortwave radiation flux. The RMSE, bias, and correlation are 37.64 $\mathrm{W m^{-2}}$, -9.82 $\mathrm{W\,m^{-2}}$, and 0.80, respectively. We observe that MAR tends to underestimate $\mathrm{SWD_{abs}} >\sim 75\ \mathrm{W\,m^{-2}}$ and does not capture any value above $> 250\ \mathrm{W\,m^{-2}}$, whereas the AWS measure values exceeding 300 $\mathrm{W\,m^{-2}}$. This underestimation of the modelled $\mathrm{SWD_{abs}}$ in the ablation zone is consistent with the modelled SMB overestimation for high ablation values (Fig. 1a–b).

Summer albedo RMSE of the MAR–OLCI-GEUS comparison (0.08) remains smaller than the observed standard deviation of 0.12. The same holds for the MAR–PROMICE & GC-NET summer albedo comparison (RMSE = 0.13 for a standard deviation of 0.22) and for the MAR–PROMICE & GC-NET summer $\mathrm{SWD_{abs}}$ comparison (RMSE = 37.64 $\mathrm{W\,m^{-2}}$ relative to observed standard deviation of 60.3 $\mathrm{W\,m^{-2}}$). This also holds for all sampled spatial resolutions (spanning 5–30 km), as listed in Table S6 and S7.

3.5 Melt extent representation

We compare the MAR-simulated melt extent at 5 km to that derived from passive microwave satellite observations (AMSR) from Picard (2025). As mentioned in Section 2.6, results are derived using a melt-threshold criterion of 0.2 $\mathrm{mm\,w.e.\,day^{-1}}$ that minimizes the model RMSE. Sensitivity tests spanning thresholds of $0.2 \pm 0.1\ \mathrm{mm\,w.e.\,day^{-1}}$ show non-significant differences (Table S8).

https://doi.org/10.5194/egusphere-2026-2341
Preprint. Discussion started: 2 July 2026

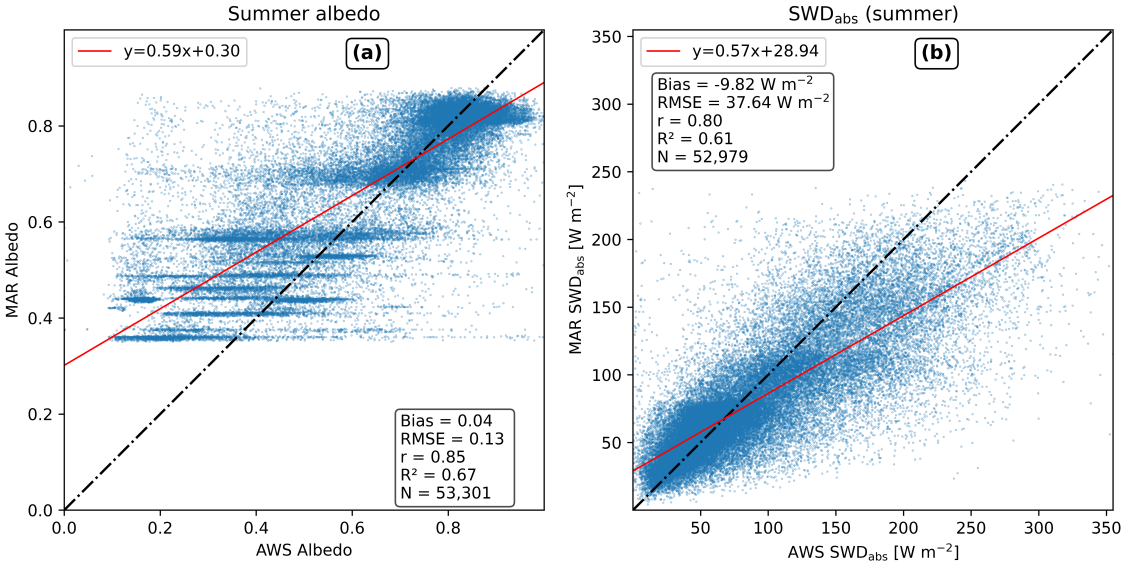

Figure 5. Comparison between modelled (MAR at 5 km) and observed (PROMICE & GC-NET AWS) summer (JJA) (a) albedo α and (b) absorbed downward shortwave radiative flux, $\mathrm{SWD_{abs}} = (1-\alpha) \times \mathrm{SWD}$. The 1:1 lines are shown as black dashed lines, and the least-squares regression lines as solid red lines. The associated statistics are reported: mean bias, root mean square error (RMSE), correlation (r), coefficient of determination (R^2) and number of observations (N).

Figure 6a reveals that observed melt days in AMSR are more frequent along the margins of the GrIS, particularly along the western margin. Figure 6b indicates that the use of a melt threshold of 0.2 $\mathrm{mm\,w.e.\,day^{-1}}$ results in an overestimation (> 30 days per year) of the mean annual number of melt days over southeastern Greenland. This region is characterized by high accumulation rates and frequent snowfall (Fettweis et al., 2020), which likely limits satellite melt detection, as fresh snow can cover underlying wet snow that would otherwise be detected as melting. Moreover, MAR suggests the presence of aquifers in this area where melt occurs sometimes 10 m or 20 m below the surface.

Besides the annual number of melt days, we also assess the timing of the onset and length of the melt season. Figure 7a not only shows that MAR accurately reproduces the onset of the melt season (around early June) as well as its ending (mid-September), but also that the timing of the peak melt extent is well captured, on average in mid-July. Focussing on the melt extent, it appears that it is slightly ($\sim$ 2–5 % of the GrIS area) overestimated during the first half of the melt season and underestimated after the peak. Regarding the maximum melt extent (shaded bands in Fig. 7a), MAR underestimates the peak value observed in summer 2012, which is reflected by the slope of the regression line in Figure 7b (<1).

Table S9 lists the results for the MAR simulations with different spatial resolutions, highlighting that RMSE increases slightly with decreasing spatial resolution (from 38,978 $\mathrm{km^2}$ at 10 km to 42,290 $\mathrm{km^2}$ at 30 km resolution).

https://doi.org/10.5194/egusphere-2026-2341
Preprint. Discussion started: 2 July 2026

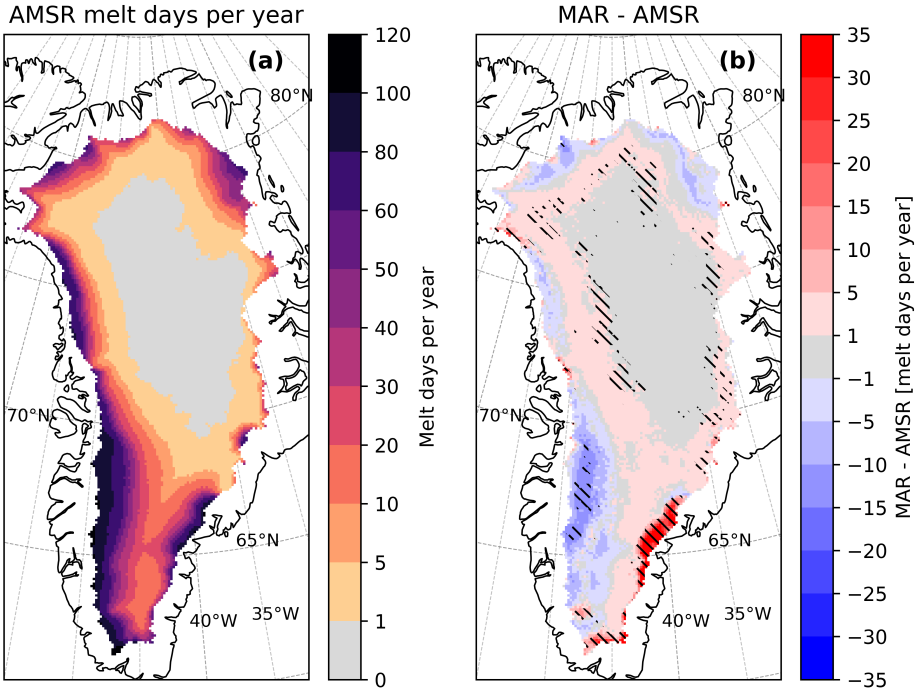

Figure 6. Mean annual number of melt days for (a) the AMSR-derived product of Picard (2025). (b) Difference in modelled and observed melt days (MAR minus AMSR), using a melt-based criterion of 0.2 $\mathrm{mm\ w.e.\ day^{-1}}$. Satellite data are derived from the ascending and descending passes (combined with "OR" criterion) of the AMRS-derived product Picard (2025) from Picard and Fily (2006). The comparison is made over the satellite data grid using an IDW interpolation. Diagonal hatching indicates grid points where the RMSE exceeds the local standard deviation of the AMSR-derived mean annual number of melt days.

3.6 SMB sensitivity to spatial resolution

In this section, we examine the differences in 1979–2024 SMB and its components across MAR simulations at resolutions spanning 5–30 km, with a focus on spatial patterns, integrated values, and interannual variability.

Figure 8 displays spatial differences in mean 1979–2024 SMB, precipitation (PR), and runoff (RU) at lower resolutions relative to the 5 km reference. The largest deviations occur at 30 km resolution, particularly in southeastern Greenland—the region with the highest accumulation rates (Fettweis et al., 2020). Here, a dipole pattern emerges with negative SMB differences along the coast and positive differences further inland. This pattern indicates that, at coarser spatial resolutions, precipitation tends to propagate further inland (Fig. 8e–h), with this inland shift increasing as resolution decreases. Unfortunately, observations in southeastern Greenland remain limited, as frequent extreme weather hampers in situ SMB measurements, thus preventing a thorough evaluation.

Along the southwestern margin, simulations at coarser resolution than 5 km exhibit positive SMB differences (mainly within one standard deviation of the 5 km variability) primarily due to reduced runoff (Fig. 8i–l).

https://doi.org/10.5194/egusphere-2026-2341
Preprint. Discussion started: 2 July 2026

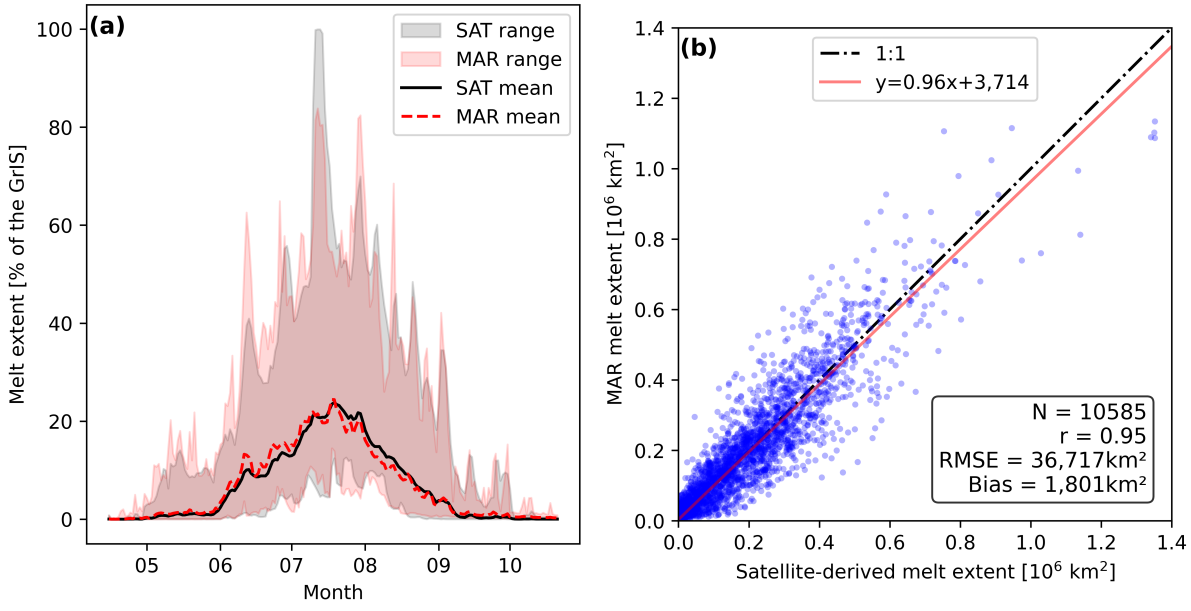

Figure 7. (a) Time series and (b) scatterplot comparing MAR modelled (red) and remotely sensed (grey) daily melt extent over the period 2002–2024. Satellite data are derived from the combined ascending and descending passes of the AMRS-derived product Picard (2025) from Picard and Fily (2006). Melt extents from MAR are obtained using a melt-based criterion of 0.2 $\mathrm{mm\,w.e.\,day^{-1}}$. In (a), shaded bands cover the minimum/maximum daily melt extent from MAR (red) and AMRS-derived melt (grey). In (b), statistics include number of record (N), correlation (r), mean bias, RMSE, slope and intercept corresponding to the least squares regression line shown in grey. The 1:1 line is blue in dash-points.

Despite some spatial noise, a consistent regional pattern emerges, particularly in the 20 and 30 km simulations: negative SMB differences are found along the southern and eastern margins of the ice sheet, relative to the 5 km simulation. By contrast, inland differences covering most of the accumulation zone, where absolute SMB values are relatively small (100–500 $\mathrm{mm\,w.e.\,year^{-1}}$, in Fig. 1a) remain limited, with absolute differences being generally below 25 $\mathrm{mm\,w.e.\,year^{-1}}$.

Root mean squared differences (RMSD) in runoff exceed the 5 km interannual variability (hatches in Fig. 8i–l) over large area, especially in the south of the GrIS accumulation zone. This primarily reflects the low runoff variability outside the ablation zone rather than large absolute differences. Within the ablation zone, runoff differences are generally smaller than the corresponding interannual variability.

Integrated differences (Table 1) show that, except at 10 km, lower resolutions produce higher integrated SMB but lower precipitation and runoff. This indicates error compensation: since precipitation and runoff have opposite signs in the SMB equation, their individual divergences partially cancel out. While integrated SMB differences remain within the 5 km interannual variability at all resolutions, this is not the case for precipitation at 15–30 km and runoff at 30 km. These discrepancies can be, in part, ascribed to smaller GrIS area and ablation zone extent as resolution coarsens (yellow contour in Fig. 8a–d),

https://doi.org/10.5194/egusphere-2026-2341
Preprint. Discussion started: 2 July 2026

Table 1. Mean 1979–2024 integrated surface mass balance (SMB), precipitation (PR), runoff (RU), ablation zone extent, GrIS area, and MARv3.14 CPU time cost. The ablation zone corresponds to regions with negative SMB. Interannual standard deviations at 5 km resolution are indicated when applicable. For each spatial resolution, we list differences relative to the 5 km reference (Δ). The numbers in parentheses represent the percentage change (relative to the reference at 5 km). CPU time at each resolution is expressed as a percentage of the reference computational cost, i.e., 31,000 minutes required to simulate one year at 5 km using 8 CPUs (AMD EPYC 7763).

	SMB [Gt yr^{-1}]	**PR** [Gt yr^{-1}]	**RU** [Gt yr^{-1}]	**Area** [10^3km^2]		CPU time [%]
Resolution				**Ablation zone**	**GrIS**	**CPU time**
5 km	**334.4**	**812.6**	**422.0**	**265**	**1,848**	**100**
standard deviation	116.6	70.3	112.7	63	–	–
Δ10 km	-2.7 (-0.8 %)	-66.0 (-8.1 %)	-56.8 (-13.5 %)	-18 (-6.8 %)	-14 (-0.8 %)	12.3
Δ15 km	26.7 (8.0 %)	-76.6 (-9.4 %)	-96.1 (-22.8 %)	-39 (-14.8 %)	-27 (-1.5 %)	3.5
Δ20 km	13.4 (4.0 %)	-96.7 (-11.9 %)	-101.7 (-24.1 %)	-41 (-15.5 %)	-34 (-1.8 %)	1.9
Δ30 km	75.8 (22.7 %)	-75.0 (-9.2 %)	-134.7 (-31.9 %)	-62 (-23.4 %)	-49 (-2.7 %)	0.5

reducing spatially integrated values, notably across inaccurately resolved GrIS margins where precipitation and runoff tend to peak.

Annual integrated values (Fig. S1) show consistent interannual variability across resolutions. However, runoff and thus SMB differences increase at lower resolutions during high-runoff years, as regression lines deviate from the 1:1 line.

Finally, the MAR vs SUMup and Ohmura and Reeh (1991) comparison at 5–30 km (Fig. 9) confirms that MAR performance improves at higher resolutions, particularly in areas experiencing high ablation (below -4 m w.e.), consistent with Fig. 8i–l. Applying the topographic correction (Fig. 9b) further improves the representation of high-ablation values. In contrast, neither resolution nor topographic correction has a significant impact on accumulation, consistent with the negligible differences observed in the central GrIS accumulation zone (Fig. 8e–h). This results from the flat inland GrIS topography that is well resolved even at low spatial resolution (Fig. S2).

4 Discussion

In the previous sections, we evaluated the latest MAR version (MARv3.14) at 5 km resolution against a set of observational data including in situ SMB (Fig. 1), meteorological (Fig. 2) and SEB (Fig. 3) records as well as albedo (Figs.4 and 5) and remotely sensed melt extent (Figs. 6 and 7). We find a general good agreement while biases remain, i.e., of the same order of magnitude as another state-of-the-art RCM at 5.5 km (RACMO2.3p2; Noël et al., 2019) for SMB, meteorological and SEB records. MAR and RACMO underestimate high ablation rates (Fig. S1c in Noël et al., 2019) and show similar agreement with meteorological and SEB measurements (Figs. S2–S3 in Noël et al., 2019) with both models underestimating high wind speeds.

https://doi.org/10.5194/egusphere-2026-2341
Preprint. Discussion started: 2 July 2026

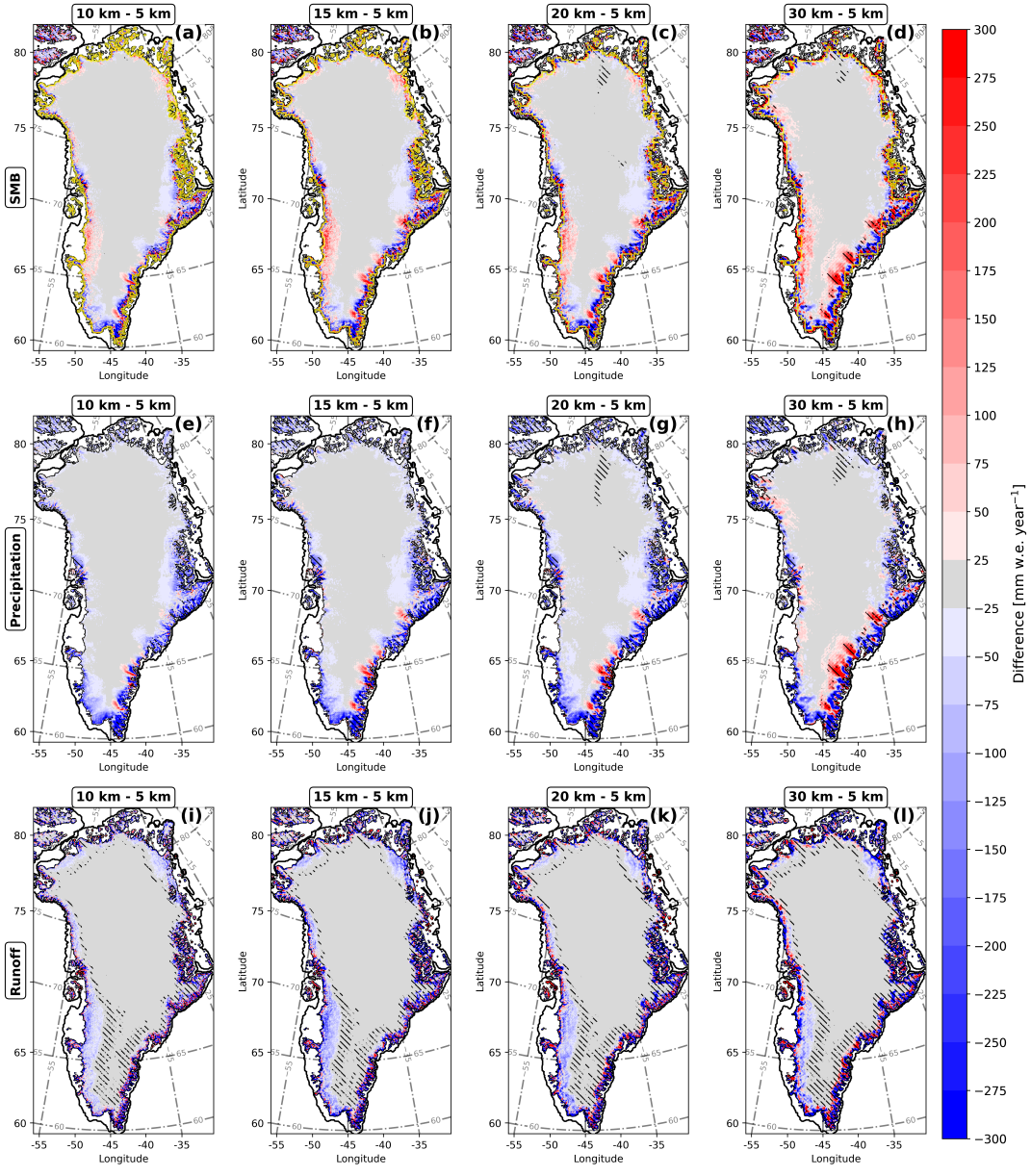

Figure 8. Differences in surface mass balance (SMB) (a–d), precipitation (snowfall plus rainfall; PR) (e–h) and runoff (RU) (i–l) between MAR at 10 km (a, e, i), 15 km (b, f, j), 20 km (c, g, k), and 30 km (d, h, l) resolution and the reference 5 km simulation, averaged over 1979–2024. All simulations were IDW interpolated onto the 5 km grid. Diagonal hatching indicates regions where the root mean squared inter-annual differences exceed the local inter-annual standard deviation at 5 km resolution (i.e. where differences are statistically significant). Yellow contour lines outline the MAR ice sheet mask at (a) 10 km, (b) 15 km, (c) 20 km, and (d) 30 km resolution.

https://doi.org/10.5194/egusphere-2026-2341
Preprint. Discussion started: 2 July 2026

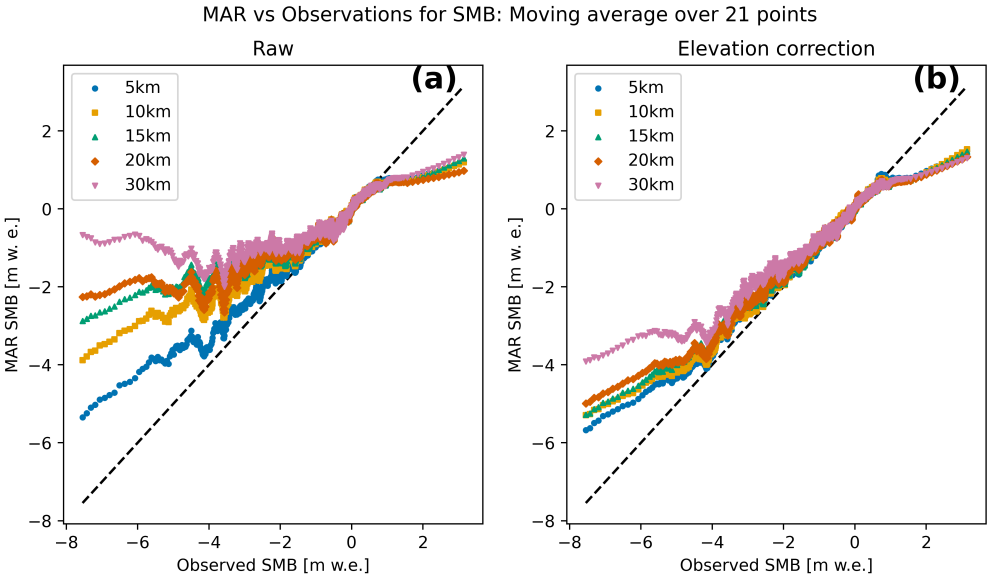

Figure 9. Scatterplots comparing modelled (MAR) and observed SMB from SUMup Vandecrux et al. (2024) and Ohmura and Reeh (1991), smoothed using a 21-points running mean. Colors and markers indicate MAR resolution: blue circles (5 km), orange squares (10 km), green upward triangles (15 km), red diamonds (20 km), and purple downward triangles (30 km). As in Figure 1b–c, MAR SMB values are computed via inverse-distance weighted (IDW) interpolation. Elevation correction is applied only in b. The black dashed line indicates the 1:1 reference line.

In the following, we examine the causes of SMB biases in MARv3.14 at 5 km. To that end, we focus on the ablation underestimation outlined in Figures 1b–c and 9 considering SEB biases at PROMICE stations. We further discuss the accumulation biases at 5 km and the inter-resolution discrepancies.

4.1 Ablation underestimate

To investigate the origin of the ablation biases at 5 km, we compare MAR to summer (JJA) SMB from pressure transducers monitored at PROMICE stations (Fig. S3b). SMB biases are then discussed considering biases in albedo, downward shortwave and longwave radiation fluxes (SWD and LWD), sensible and latent heat fluxes (SHF and LHF), near-surface temperature (T) and wind speed (WS) computed at PROMICE stations over the exact same periods (Table 2). Only uninterrupted measurement periods longer than 30 days are retained.

Interestingly, the comparison with pressure transducer data (Figure S3a) yields similar results to those shown in Figure 1b, despite the smaller sample size (137 vs 3012 points in Fig. 1). The RMSE is 0.56 m w.e. (vs 0.51 m w.e.), the correlation is unchanged, and the mean bias is slightly higher at 0.33 m w.e. (vs 0.10 m w.e.), for an observed standard deviation of 1.20 m w.e. (vs 1.29 m w.e.). Hereafter, we discuss pressure transducer sites (Fig. S3b) from north to south.

https://doi.org/10.5194/egusphere-2026-2341
Preprint. Discussion started: 2 July 2026

For the two stations located in northwestern Greenland (THU_L and THU_U, standing for lower and upper sites), MAR underestimates ablation, notably at THU_L, primarily due to an overestimation of albedo. Although SWD is itself underestimated, the albedo bias has a stronger impact. Typical summer SWD ($250\ \mathrm{W\,m^{-2}}$) implies that an albedo bias of 0.1 induces an error of $25\ \mathrm{W\,m^{-2}}$, corresponding to $7\ \mathrm{mm\,w.e.\,day^{-1}}$ of melt. LWD is also underestimated, likely due to cloud cover underestimate. In addition, SHF is particularly underestimated at THU_L, consistent with too low wind speed, further contributing to the ablation underestimate.

For the two central-western stations (UPE_L and UPE_U), contrasting behaviours are observed. UPE_L is the only station where MAR overestimates ablation, and among the few stations where albedo is underestimated. At this site, the sum of radiative biases amounts to approximately +2.5 $\mathrm{W\,m^{-2}}$. However, while this radiative bias should result in an ablation overestimation of only $\sim 0.7\ \mathrm{mm\,w.e.}$, we observe a bias of $\sim 2\ \mathrm{mm\,w.e.}$. This discrepancy highlights that SEB biases cannot be directly translated into ablation biases using a simple thermodynamic relationship. Additional biases, such as in precipitation, drifting snow erosion and deposition, sublimation, and measurement uncertainties, may also play a role.

In central-eastern Greenland, both SCO_L and SCO_U exhibit the largest albedo overestimate (up to 0.18), leading to substantial underestimation of absorbed shortwave radiation ($\mathrm{SWD_{abs}}$). These stations are characterized by low bare-ice albedo values (approximately 0.4) not captured by MAR at $5\ \mathrm{km}$. As these stations lie within a glacial valley, interpolation of MAR topography leads to an elevation overestimation ($> 300\ \mathrm{m}$). Despite this, near-surface temperature is not underestimated. Wind speed, however, is underestimated, leading to an underestimation of the SHF and, consequently, of melt thus explaining SMB overestimate.

At the KAN_L and KAN_M stations located in the southwestern Greenland, MAR overestimates SMB. Along with UPE_L, KAN_L underestimates albedo, likely resulting from a combination of underestimated snowfall and a too early transition from snow to bare ice.

MAR exhibits similar biases in SMB and SEB fluxes at KAN_M and NUK_U, with an underestimation of $\mathrm{SWD_{abs}}$ and LWD, and an overestimation of both the SHF and LHF. Note that, these biases are smaller at NUK_U.

In southeast Greenland, stations TAS_A and TAS_L illustrate model error compensation. There, the underestimation of $\mathrm{SWD_{abs}}$ and LWD is partly offset by an overestimation of SHF, resulting in one of the smallest SMB biases ($1.4\ \mathrm{mm\,w.e.\,day^{-1}}$ at TAS_A). More generally, MAR underestimates ablation at both TAS stations.

Finally, at the southern stations QAS_L and QAS_M, MAR overestimates albedo (by up to 0.17 at QAS_L), resulting in too high SMB. In addition, LWD is slightly underestimated, whereas SHF and LHF are slightly overestimated.

Overall, the primary driver of ablation underestimation is the overestimation of bare-ice albedo. As discussed in Antwerpen et al. (2022), bare-ice albedo is strongly influenced by light-absorbing constituents (LACs), such as dust, black carbon, organic matter, and algae, as well as by the presence of supraglacial lakes (Wu et al., 2025). These processes are not explicitly represented in regional climate models, motivating the use of MODIS-based bare-ice albedo prescriptions in MARv3.14. While prescribing albedo improves spatial variability relative to earlier configurations using nearly constant values, it does not capture short-term and local fluctuations. Post-processing corrections can improve bare-ice albedo representation, but are not applicable for SMB projections.

https://doi.org/10.5194/egusphere-2026-2341
Preprint. Discussion started: 2 July 2026

Beyond albedo effects, summer downward radiative fluxes remain underestimated at 5 km resolution (Fig. 3a,b). The implementation of a new radiative scheme in the latest MAR version has not significantly improved their representation (Table S5), suggesting that the remaining biases are likely related to inaccurate cloud and fog representation.

Table 2. Bias in modelled summer (JJA) surface mass balance (SMB) relative to PROMICE pressure-transducer measurements (MAR - observations; positive values indicate an underestimation of melt by MAR) in $\mathrm{mm\,w.e.\,day^{-1}}$ (2009–2023). Biases in albedo (α), downward shortwave radiation (SWD), absorbed shortwave radiation (i.e., $\mathrm{SWD_{abs} = (1-\alpha) \times SWD}$), downward longwave radiation (LWD), sensible and latent heat fluxes (SHF and LHF), near-surface air temperature (T), and wind speed (WS) are also listed. All biases are computed over the exact same periods as the SMB measurements. Measurements periods shorter than 30 days were discarded. Δz is the altitude difference between the station and the MAR IDW-interpolated elevation at the same location. N denotes the cumulative number of days of observation for each station. Note that a forcing of 1 $\mathrm{W\,m^{-2}}$ corresponds to a melt rate of 0.28 $\mathrm{mm\,w.e.\,day^{-1}}$ (Appendix B).

Station	Lon	Lat	SMB	α	SWD	$\mathrm{SWD_{abs}}$	LWD	SHF	LHF	T	WS	Δz	N
			$\mathrm{mm\,w.e.\,d^{-1}}$	–			$\mathrm{W\,m^{-2}}$			°C	$\mathrm{m\,s^{-1}}$	m	
THU_L	-68.3	76.4	7.7	0.12	-10.1	-32.2	-12.9	-33.2	0.4	0.8	-1.2	-25	212
THU_U	-68.1	76.4	1.8	0.05	4.3	-5.5	-17.1	-9.0	-1.6	-1.0	-1.4	-26	49
UPE_L	-54.3	72.9	-2.0	-0.03	-5.7	3.9	-9.1	1.9	5.8	-1.8	0.3	-8	632
UPE_U	-53.5	72.9	5.1	0.09	-10.1	-26.1	-8.5	-1.0	6.9	-0.7	-0.4	5	378
SCO_L	-26.8	72.2	14.0	0.18	1.6	-42.1	-10.9	-26.9	1.0	1.9	-0.6	475	336
SCO_U	-27.3	72.4	11.1	0.18	-23.7	-54.0	0.6	-10.2	5.9	0.0	-1.4	212	370
KAN_L	-49.9	67.1	3.2	-0.03	-7.8	2.0	-10.3	6.7	5.1	-1.3	0.5	-11	811
KAN_M	-48.8	67.1	3.6	0.12	-4.9	-31.5	-6.8	7.6	4.7	0.2	0.0	13	193
NUK_U	-49.3	64.5	2.9	0.07	-3.2	-16.9	-0.9	8.6	0.3	-0.2	0.3	-1	178
TAS_A	-38.9	65.8	1.4	0.14	-4.9	-38.2	-14.4	19.9	-1.7	-1.3	1.0	10	51
TAS_L	-38.9	65.6	4.9	0.11	-10.5	-34.8	-4.1	6.7	1.8	0.1	-0.3	3	85
QAS_L	-46.9	61.0	2.4	0.17	-0.7	-37.7	-5.4	1.8	4.1	-0.4	-0.3	23	237
QAS_M	-46.8	61.1	7.6	0.09	12.7	-9.8	-11.2	9.4	8.9	-0.3	-0.4	12	91

4.2 Accumulation biases

As in previous studies (e.g. Fettweis et al., 2020), SMB evaluation remains limited in southeastern Greenland, where extreme weather conditions hinder in situ observations. However, airborne radar measurements indicate that MAR tends to overestimate accumulation (by up to 1 $\mathrm{m\,w.e.\,year^{-1}}$) in this region, even more than RACMO or HIRHAM (Koenig et al., 2016). This result is supported by Lindsey-Clark et al. (2025), who evaluated MARv3.14 against radar-derived accumulation. We therefore refer to that study for a detailed discussion of the model's accumulation biases. Besides, the accumulation in the ice sheet interior is underestimated by MAR (Figs. 1 and S1). These two findings suggest an overestimation of the orographic barrier effect by the model, resulting in too high accumulation over the rugged GrIS margins with too low precipitation inland.

https://doi.org/10.5194/egusphere-2026-2341
Preprint. Discussion started: 2 July 2026

4.3 Impact of spatial resolution

We demonstrate that the spatial resolution at which MAR is run can significantly affect modelled SMB (ranging from -0.8 % at 10 km to +22.7 % at 30 km relative to the 5 km reference; Table 1). Specifically, for ablation, we find that coarse resolutions cannot capture high marginal runoff rates without topographic correction. In fact, coarser resolutions simulate lower integrated runoff (ranging from -13 % at 10 km to -32 % at 30 km), in line with an underestimate of the ablation zone extent. The higher the integrated runoff, the higher the inter-resolution discrepancies (Fig. S1). Differences also occur in the accumulation zone where discrepancies also emerge at lower resolution, particularly in the southeastern GrIS. Integrated, the accumulation differences range from -8 % at 10 km to -12 % at 20 km.

Overall, our inter-resolution comparison highlights the rugged GrIS margins—where SMB gradients are strongest as main driver of discrepancies between resolutions. In line with Franco et al. (2012), the loss of spatial detail in rugged marginal regions, rather than differences over the flat GrIS interior, where SMB fields are comparatively smooth and largely resolution-insensitive, is the dominant process control of integrated SMB discrepancies.

These discrepancies are most pronounced at coarse resolution—particularly at 30 km—and in the southeastern GrIS (Fig. S2). There, coarser grids smooth the topography along the GrIS margins, reducing the orographic barrier effect, hence facilitating moisture transport toward the ice sheet interior (Fig. 8h).

In view of our results, MAR at 10 km makes a relevant trade-off between model performance and computational cost, as it yields results consistent with the 5 km reference (Table 1 and Fig. 9) for only 12 % of its CPU time requirements (Table 1). Indeed, 10 km is the only resolution at which MAR integrated SMB (components) do not significantly differ to those of the 5 km reference, i.e., model differences lower than the interannual variability (standard deviation; Table 1).

MAR at 10 km could be further enhanced by implementing sub-pixels that sample SMB components at different elevation within a single MAR grid-cell. Such approach is similar to elevation classes incorporated in e.g. Earth System Models (Sellevold et al., 2019) and is currently under development in MAR.

5 Conclusions

We evaluate MARv3.14 at 5 km over the GrIS for the present climate (1979–2024), using a broad range of observational datasets, including in situ SMB measurements, meteorological and SEB variables recorded at AWSs, remotely sensed albedo, and melt extent. We further assess the impact of spatial resolution on SMB simulations. We find that MAR SMB agrees well with in situ observations, showing an RMSE of 0.51 m w.e. and a correlation of 0.93. A slight underestimation of ablation persists, largely related to biases in bare-ice albedo, which remains difficult to correct given unresolved surface impurities and biological processes in MAR. Differences between resolutions increase as grid spacing coarsens, but these discrepancies can be reduced through topographic correction or the implementation of sub-pixels in MAR. Running MAR at 10 km makes a suitable compromise for long-term climate projections, yielding results in line with the reference 5 km simulation, while requiring only 12 % of its computational cost.

https://doi.org/10.5194/egusphere-2026-2341
Preprint. Discussion started: 2 July 2026

Remaining SMB biases at 5 km are primarily driven by inaccurate representation of bare-ice albedo, cloud cover and surface topography. Therefore, future developments should prioritize improving the representation of clouds and associated precipitation, which directly affects both radiative fluxes and accumulation. Existing studies based on radar-derived accumulation rates provide valuable additional constraints and could further support model evaluation in regions where in situ measurements are sparse.

Appendix A: Inverse distance weighting interpolation

Denoting SMB_i as the four modelled SMB values (summed over the matching periods) closest to each SMB measurement, the corresponding MAR value ($\mathrm{SMB}_{\mathrm{IDW}}$) is estimated as (Eq. A1):

$$\mathrm{SMB}_{\mathrm{IDW}} = \frac{\sum_{i=1}^{4} w_i \,\mathrm{SMB}_i}{\sum_{i=1}^{4} w_i}, \qquad w_i = d_i^{-2}, \tag{A1}$$

where d_i is the horizontal distance between the measurement site and MAR grid cell i.

Appendix B: Conversion of surface energy budget biases into melt biases

The energy required to melt ice is given by

$$Q = mL_f, \tag{B1}$$

where Q is the energy [J], m the melted ice mass [kg], and $L_f \approx 3.335 \times 10^5\ \mathrm{J\,kg^{-1}}$ is the latent heat of fusion.

A radiative flux F [$\mathrm{W\,m^{-2}}$] applied over a surface S [$\mathrm{m^2}$] during a time interval Δt [s] provides an energy

$$Q = FS\Delta t. \tag{B2}$$

This energy is used to melt a layer of ice of thickness Δz [m], such that

$$m = \rho S \Delta z, \tag{B3}$$

where ρ is the density of ice [$\mathrm{kg\,m^{-3}}$].

Combining the above expressions yields

$$FS\Delta t = \rho S \Delta z L_f, \tag{B4}$$

which simplifies to

$$\Delta z = \frac{F\Delta t}{\rho L_f}. \tag{B5}$$

https://doi.org/10.5194/egusphere-2026-2341
Preprint. Discussion started: 2 July 2026

For a daily timescale ($\Delta t = 86400$ s), the melt rate becomes

$$\frac{\Delta z}{\Delta t} = \frac{F}{\rho L_f}, \quad \Rightarrow \quad \Delta z_{\text{day}} = F \frac{86400}{\rho L_f}. \tag{B6}$$

Using $\rho = 917\ \text{kg m}^{-3}$ and $L_f = 3.335 \times 10^5\ \text{J kg}^{-1}$, a radiative bias of

$$F = 1\ \text{W m}^{-2} \tag{B7}$$

corresponds to a melt rate of approximately

$$\Delta z \approx 0.28\ \text{mm day}^{-1}. \tag{B8}$$

Data availability. MARv3.14 outputs at 5 km resolution are available at https://doi.org/10.5281/zenodo.19691263, those at 10 km are available at http://ftp.climato.be/fettweis/MARv3.14/Greenland/ERA5-10km-daily/ (last accessed 04/23/2026). OLCI-GEUS albedo products are available at https://dataverse.geus.dk/dataverse/sice, PROMICE & GC-NET data is available at https://promice.org/download-data/, Melt extent data is available at https://snow.univ-grenoble-alpes.fr/melting/, and SUMup data is available at https://arcticdata.io/catalog/view/doi:10.18739/A2M61BR5M.

Author contributions. GT, BN and XF designed the study. GT conducted data analysis. XF carried out the MAR simulations at different resolutions. All authors commented on the paper.

Competing interests. At least one of the (co-)authors is a member of the editorial board of The Cryosphere.

Acknowledgements. G. Timmermans is a research fellow of the Fonds de la Recherche Scientifique de Belgique F.R.S-FNRS. B. Noël is a research associate of the Fonds de la Recherche Scientifique de Belgique F.R.S-FNRS. C. Kittel is a postdoc fellow of the Fonds de la Recherche Scientifique de Belgique F.R.S–FNRS. Computational resources have been provided by the Consortium des Équipements de Calcul Intensif (CÉCI), funded by the Fonds de la Recherche Scientifique de Belgique (F.R.S.-FNRS) under Grant No. 2.5020.11 and by the Walloon Region

Data from the Programme for Monitoring of the Greenland Ice Sheet (PROMICE) are provided by the Geological Survey of Denmark and Greenland (GEUS) at http://www.promice.dk. ZAC, LYN, FRE and NUK_K stations are financially supported by the Glaciobasis programme as part of the Greenland Ecosystem Monitoring project (https://g-e-m.dk/). The NUK_K station is serviced by Asiaq Greenland Survey. The WEG stations are paid for and maintained by Jakob Abermann at the Department of Geography and Regional Science of the University of Graz. The RED_Lv3 station is financed and maintained by Rainer Prinz at the Department of Atmospheric and Cryospheric Sciences of the University of Innsbruck. The SER_B station is paid for and serviced by Anders Bjørk at the Department of Geosciences and Natural Resource Management of the University of Copenhagen. We thank Ghislain Picard for making his melt extent data that open access. We

https://doi.org/10.5194/egusphere-2026-2341
Preprint. Discussion started: 2 July 2026

thank Chloë Paice, Clara Lambin and Damien Maure for their advice during the writing, as well as Jean-François Grailet for IT advice, and Alison Delhasse for sharing her MARv3.9 dataset.

https://doi.org/10.5194/egusphere-2026-2341
Preprint. Discussion started: 2 July 2026

References

Amory, C., Kittel, C., Le Toumelin, L., Agosta, C., Delhasse, A., Favier, V., and Fettweis, X.: Performance of MAR (v3.11) in simulating the drifting-snow climate and surface mass balance of Adélie Land, East Antarctica, Geoscientific Model Development, 14, 3487–3510, https://doi.org/10.5194/gmd-14-3487-2021, 2021.

Antwerpen, R. M., Tedesco, M., Fettweis, X., Alexander, P., and van de Berg, W. J.: Assessing bare-ice albedo simulated by MAR over the Greenland ice sheet (2000–2021) and implications for meltwater production estimates, The Cryosphere, 16, 4185–4199, https://doi.org/10.5194/tc-16-4185-2022, 2022.

Box, J. E. and Rinke, A.: Evaluation of Greenland Ice Sheet Surface Climate in the HIRHAM Regional Climate Model Using Automatic Weather Station Data, Journal of Climate, 16, 1302 – 1319, https://doi.org/10.1175/1520-0442(2003)16<1302:EOGISS>2.0.CO;2, 2003.

Brajkovic, J., Fettweis, X., Noël, B., Vyver, H. V. D., Ghilain, N., Archambeau, P., Pirotton, M., and Doutreloup, S.: Increased intensity and frequency of extreme precipitation events in Belgium as simulated by the regional climate model MAR, Journal of Hydrology: Regional Studies, 59, 102 399, https://doi.org/https://doi.org/10.1016/j.ejrh.2025.102399, 2025.

Choi, Y., Morlighem, M., Rignot, E., and Wood, M.: Ice dynamics will remain a primary driver of Greenland ice sheet mass loss over the next century, 2, 26, https://doi.org/10.1038/s43247-021-00092-z, 2021.

De Ridder, K. and Gallée, H.: Land Surface–Induced Regional Climate Change in Southern Israel, Journal of Applied Meteorology, 37, 1470 – 1485, https://doi.org/10.1175/1520-0450(1998)037<1470:LSIRCC>2.0.CO;2, 1998.

Delhasse, A., Kittel, C., Amory, C., Hofer, S., van As, D., S. Fausto, R., and Fettweis, X.: Brief communication: Evaluation of the near-surface climate in ERA5 over the Greenland Ice Sheet, The Cryosphere, 14, 957–965, https://doi.org/10.5194/tc-14-957-2020, 2020.

Delhasse, A., Beckmann, J., Kittel, C., and Fettweis, X.: Coupling MAR (Modèle Atmosphérique Régional) with PISM (Parallel Ice Sheet Model) mitigates the positive melt–elevation feedback, The Cryosphere, 18, 633–651, https://doi.org/10.5194/tc-18-633-2024, 2024.

Dethinne, T., Glaude, Q., Picard, G., Kittel, C., Alexander, P., Orban, A., and Fettweis, X.: Sensitivity of the MAR regional climate model snowpack to the parameterization of the assimilation of satellite-derived wet-snow masks on the Antarctic Peninsula, The Cryosphere, 17, 4267–4288, https://doi.org/10.5194/tc-17-4267-2023, 2023.

Doutreloup, S., Wyard, C., Amory, C., Kittel, C., Erpicum, M., and Fettweis, X.: Sensitivity to Convective Schemes on Precipitation Simulated by the Regional Climate Model MAR over Belgium (1987–2017), Atmosphere, 10, https://doi.org/10.3390/atmos10010034, 2019.

Enderlin, E. M., Howat, I. M., Jeong, S., Noh, M.-J., Van Angelen, J. H., and Van Den Broeke, M. R.: An improved mass budget for the Greenland ice sheet, Geophysical Research Letters, 41, 866–872, 2014.

Ernotte, R.: Comparaison entre l'estimation de l'albedo en surface de MAR et les valeurs d'albedo reconstituées à partir du capteur OLCI de Sentinel-3 (étude de cas de la calotte glaciaire du Groenland en 2018 et 2019), https://matheo.uliege.be/handle/2268.2/22271, supervised by Xavier Fettweis and Quentin Glaude, 2025.

Fausto, R. S., van As, D., Mankoff, K. D., Vandecrux, B., Citterio, M., Ahlstrøm, A. P., Andersen, S. B., Colgan, W., Karlsson, N. B., Kjeldsen, K. K., Korsgaard, N. J., Larsen, S. H., Nielsen, S., Pedersen, A. Ø., Shields, C. L., Solgaard, A. M., and Box, J. E.: Programme for Monitoring of the Greenland Ice Sheet (PROMICE) automatic weather station data, Earth System Science Data, 13, 3819–3845, https://doi.org/10.5194/essd-13-3819-2021, 2021.

Fettweis, X.: Reconstruction of the 1979ndash;2006 Greenland ice sheet surface mass balance using the regional climate model MAR, The Cryosphere, 1, 21–40, https://doi.org/10.5194/tc-1-21-2007, 2007.

https://doi.org/10.5194/egusphere-2026-2341
Preprint. Discussion started: 2 July 2026

Fettweis, X., Gallée, H., Lefebre, F., and van Ypersele, J.-P.: Greenland surface mass balance simulated by a regional climate model and comparison with satellite-derived data in 1990–1991, Climate Dynamics, 24, 632–640, https://doi.org/https://doi.org/10.1007/s00382-005-0010-y, 2005.

Fettweis, X., Gallée, H., Lefebre, F., and van Ypersele, J.-P.: The 1988–2003 Greenland ice sheet melt extent using passive microwave satellite data and a regional climate model, Climate Dynamics, 27, 531–541, https://doi.org/https://doi.org/10.1007/s00382-006-0150-8, 2006.

Fettweis, X., Tedesco, M., van den Broeke, M., and Ettema, J.: Melting trends over the Greenland ice sheet (1958–2009) from spaceborne microwave data and regional climate models, The Cryosphere, 5, 359–375, https://doi.org/10.5194/tc-5-359-2011, 2011.

Fettweis, X., Franco, B., Tedesco, M., van Angelen, J. H., Lenaerts, J. T. M., van den Broeke, M. R., and Gallée, H.: Estimating the Greenland ice sheet surface mass balance contribution to future sea level rise using the regional atmospheric climate model MAR, The Cryosphere, 7, 469–489, https://doi.org/10.5194/tc-7-469-2013, 2013.

Fettweis, X., Box, J. E., Agosta, C., Amory, C., Kittel, C., Lang, C., van As, D., Machguth, H., and Gallée, H.: Reconstructions of the 1900–2015 Greenland ice sheet surface mass balance using the regional climate MAR model, The Cryosphere, 11, 1015–1033, https://doi.org/10.5194/tc-11-1015-2017, 2017.

Fettweis, X., Hofer, S., Krebs-Kanzow, U., Amory, C., Aoki, T., Berends, C. J., Born, A., Box, J. E., Delhasse, A., Fujita, K., Gierz, P., Goelzer, H., Hanna, E., Hashimoto, A., Huybrechts, P., Kapsch, M.-L., King, M. D., Kittel, C., Lang, C., Langen, P. L., Lenaerts, J. T. M., Liston, G. E., Lohmann, G., Mernild, S. H., Mikolajewicz, U., Modali, K., Mottram, R. H., Niwano, M., Noël, B., Ryan, J. C., Smith, A., Streffing, J., Tedesco, M., van de Berg, W. J., van den Broeke, M., van de Wal, R. S. W., van Kampenhout, L., Wilton, D., Wouters, B., Ziemen, F., and Zolles, T.: GrSMBMIP: intercomparison of the modelled 1980–2012 surface mass balance over the Greenland Ice Sheet, The Cryosphere, 14, 3935–3958, https://doi.org/10.5194/tc-14-3935-2020, 2020.

Fettweis, X., B., A., P.M, D., Ghilain, N., P., P., and C., W.: Évolution actuelle (1960-2021) de l'enneigement dans les Vosges à l'aide du modèle régional du climat MAR, Bulletin de la Société Géographique de Liège, 80, https://doi.org/10.25518/0770-7576.7049, 2023.

Franco, B., Fettweis, X., Lang, C., and Erpicum, M.: Impact of spatial resolution on the modelling of the Greenland ice sheet surface mass balance between 1990–2010, using the regional climate model MAR, The Cryosphere, 6, 695–711, https://doi.org/10.5194/tc-6-695-2012, 2012.

Franco, B., Fettweis, X., and Erpicum, M.: Future projections of the Greenland ice sheet energy balance driving the surface melt, The Cryosphere, 7, 1–18, https://doi.org/10.5194/tc-7-1-2013, 2013.

Fridlind, A. M., Ackerman, A. S., McFarquhar, G., Zhang, G., Poellot, M. R., DeMott, P. J., Prenni, A. J., and Heymsfield, A. J.: Ice properties of single-layer stratocumulus during the Mixed-Phase Arctic Cloud Experiment: 2. Model results, Journal of Geophysical Research: Atmospheres, 112, https://doi.org/https://doi.org/10.1029/2007JD008646, 2007.

Fürst, J. J., Goelzer, H., and Huybrechts, P.: Ice-dynamic projections of the Greenland ice sheet in response to atmospheric and oceanic warming, The Cryosphere, 9, 1039–1062, https://doi.org/10.5194/tc-9-1039-2015, 2015.

Gallée, H. and Schayes, G.: Development of a three-dimensional meso-γ primitive equation model: katabatic winds simulation in the area of Terra Nova Bay, Antarctica, Monthly Weather Review, 122, 671–685, https://doi.org/10.1175/1520-0493(1994)122<0671:DOATDM>2.0.CO;2, 1994.

Glaude, Q., Noel, B., Olesen, M., Van den Broeke, M., van de Berg, W. J., Mottram, R., Hansen, N., Delhasse, A., Amory, C., Kittel, C., Goelzer, H., and Fettweis, X.: A Factor Two Difference in 21st-Century Greenland Ice Sheet Surface Mass Balance Projections From

https://doi.org/10.5194/egusphere-2026-2341
Preprint. Discussion started: 2 July 2026

Three Regional Climate Models Under a Strong Warming Scenario (SSP5-8.5), Geophysical Research Letters, 51, e2024GL111 902, https://doi.org/https://doi.org/10.1029/2024GL111902, e2024GL111902 2024GL111902, 2024.

Goelzer, H., Huybrechts, P., Fürst, J. J., Nick, F. M., Andersen, M. L., Edwards, T. L., Fettweis, X., Payne, A. J., and Shannon, S.: Sensitivity of Greenland ice sheet projections to model formulations, Journal of Glaciology, 59, 733–749, 2013.

Goelzer, H., Nowicki, S., Payne, A., Larour, E., Seroussi, H., Lipscomb, W. H., Gregory, J., Abe-Ouchi, A., Shepherd, A., Simon, E., Agosta, C., Alexander, P., Aschwanden, A., Barthel, A., Calov, R., Chambers, C., Choi, Y., Cuzzone, J., Dumas, C., Edwards, T., Felikson, D., Fettweis, X., Golledge, N. R., Greve, R., Humbert, A., Huybrechts, P., Le clec'h, S., Lee, V., Leguy, G., Little, C., Lowry, D. P., Morlighem, M., Nias, I., Quiquet, A., Rückamp, M., Schlegel, N.-J., Slater, D. A., Smith, R. S., Straneo, F., Tarasov, L., van de Wal, R., and van den Broeke, M.: The future sea-level contribution of the Greenland ice sheet: a multi-model ensemble study of ISMIP6, The Cryosphere, 14, 3071–3096, https://doi.org/10.5194/tc-14-3071-2020, 2020.

Grailet, J.-F., Hogan, R. J., Ghilain, N., Bolsée, D., Fettweis, X., and Grégoire, M.: Inclusion of the ECMWF ecRad radiation scheme (v1.5.0) in the MAR (v3.14), regional evaluation for Belgium, and assessment of surface shortwave spectral fluxes at Uccle, Geoscientific Model Development, 18, 1965–1988, https://doi.org/10.5194/gmd-18-1965-2025, 2025.

Haacker, J., Wouters, B., Fettweis, X., Glissenaar, I. A., and Box, J. E.: Atmospheric-river-induced foehn events drain glaciers on Novaya Zemlya, Nature Communications, 15, 7021, https://doi.org/10.1038/s41467-024-51404-8, 2024.

Hersbach, H., Bell, B., Berrisford, P., Hirahara, S., Horányi, A., Muñoz-Sabater, J., Nicolas, J., Peubey, C., Radu, R., Schepers, D., Simmons, A., Soci, C., Abdalla, S., Abellan, X., Balsamo, G., Bechtold, P., Biavati, G., Bidlot, J., Bonavita, M., De Chiara, G., Dahlgren, P., Dee, D., Diamantakis, M., Dragani, R., Flemming, J., Forbes, R., Fuentes, M., Geer, A., Haimberger, L., Healy, S., Hogan, R. J., Hólm, E., Janisková, M., Keeley, S., Laloyaux, P., Lopez, P., Lupu, C., Radnoti, G., de Rosnay, P., Rozum, I., Vamborg, F., Villaume, S., and Thépaut, J.-N.: The ERA5 global reanalysis, Quarterly Journal of the Royal Meteorological Society, 146, 1999–2049, https://doi.org/https://doi.org/10.1002/qj.3803, 2020.

Hogan, R. J. and Bozzo, A.: A Flexible and Efficient Radiation Scheme for the ECMWF Model, Journal of Advances in Modeling Earth Systems, 10, 1990–2008, https://doi.org/https://doi.org/10.1029/2018MS001364, 2018.

How, P., Abermann, J., Ahlstrøm, A., Andersen, S., Box, J., Citterio, M., Colgan, W., Fausto, R., Karlsson, N., Jakobsen, J., et al.: PROMICE and GC-Net automated weather station data in Greenland, GEUS Dataverse, 8, 2022.

IMBIE: Mass balance of the Greenland Ice Sheet from 1992 to 2018, Nature, 579, 233–239, 2020.

Karlsson, N. B., Eisen, O., Dahl-Jensen, D., Freitag, J., Kipfstuhl, S., Lewis, C., Nielsen, L. T., Paden, J. D., Winter, A., and Wilhelms, F.: Accumulation Rates during 1311–2011 CE in North-Central Greenland Derived from Air-Borne Radar Data, Frontiers in Earth Science, Volume 4 - 2016, https://doi.org/10.3389/feart.2016.00097, 2016.

Karlsson, N. B., Razik, S., Hörhold, M., Winter, A., Steinhage, D., Binder, T., and Eisen, O.: Surface accumulation in Northern Central Greenland during the last 300 years, Annals of Glaciology, 61, 214–224, https://doi.org/10.1017/aog.2020.30, 2020.

Kittel, C., Amory, C., Agosta, C., Delhasse, A., Doutreloup, S., Huot, P.-V., Wyard, C., Fichefet, T., and Fettweis, X.: Sensitivity of the current Antarctic surface mass balance to sea surface conditions using MAR, The Cryosphere, 12, 3827–3839, https://doi.org/10.5194/tc-12-3827-2018, 2018.

Kittel, C., Amory, C., Agosta, C., Jourdain, N. C., Hofer, S., Delhasse, A., Doutreloup, S., Huot, P.-V., Lang, C., Fichefet, T., and Fettweis, X.: Diverging future surface mass balance between the Antarctic ice shelves and grounded ice sheet, The Cryosphere, 15, 1215–1236, https://doi.org/10.5194/tc-15-1215-2021, 2021.

https://doi.org/10.5194/egusphere-2026-2341
Preprint. Discussion started: 2 July 2026

Koenig, L. S., Ivanoff, A., Alexander, P. M., MacGregor, J. A., Fettweis, X., Panzer, B., Paden, J. D., Forster, R. R., Das, I., McConnell, J. R., Tedesco, M., Leuschen, C., and Gogineni, P.: Annual Greenland accumulation rates (2009–2012) from airborne snow radar, The Cryosphere, 10, 1739–1752, https://doi.org/10.5194/tc-10-1739-2016, 2016.

Lang, C., Fettweis, X., and Erpicum, M.: Stable climate and surface mass balance in Svalbard over 1979ndash;2013 despite the Arctic warming, The Cryosphere, 9, 83–101, https://doi.org/10.5194/tc-9-83-2015, 2015.

Langen, P. L., Fausto, R. S., Vandecrux, B., Mottram, R. H., and Box, J. E.: Liquid Water Flow and Retention on the Greenland Ice Sheet in the Regional Climate Model HIRHAM5: Local and Large-Scale Impacts, Frontiers in Earth Science, Volume 4 - 2016, https://doi.org/10.3389/feart.2016.00110, 2017.

Leduc-Leballeur, M., Picard, G., Zeiger, P., and Macelloni, G.: Empirical classification of dry-wet snow status in Antarctica using multi-frequency passive microwave observations, The Cryosphere, 20, 1199–1216, https://doi.org/10.5194/tc-20-1199-2026, 2026.

Lenaerts, J. T. M., Medley, B., van den Broeke, M. R., and Wouters, B.: Observing and Modeling Ice Sheet Surface Mass Balance, Reviews of Geophysics, 57, 376–420, https://doi.org/https://doi.org/10.1029/2018RG000622, 2019.

Lindsey-Clark, J. Y., Grinsted, A., Vandecrux, B., and Schøtt Hvidberg, C.: Greenland Monthly Accumulation Maps (1960–2022): A Statistical Semi-Empirical Bias-Adjustment Model, EGUsphere, 2025, 1–45, https://doi.org/10.5194/egusphere-2025-2516, 2025.

Luetzenburg, G., Korsgaard, N. J., Deichmann, A. K., Socher, T., Gleie, K., Scharffenberger, T., Fahrner, D., Nielsen, E. B., How, P., Bjørk, A. A., Kjeldsen, K. K., Ahlstrøm, A. P., and Fausto, R. S.: PROMICE-2022 Ice Mask, https://doi.org/10.22008/FK2/O8CLRE, 2025.

Macé, L., Vandenbulcke, L., Brankart, J.-M., Brasseur, P., and Grégoire, M.: Characterisation of uncertainties in an ocean radiative transfer model for the Black Sea through ensemble simulations, Biogeosciences, 22, 3747–3768, https://doi.org/10.5194/bg-22-3747-2025, 2025.

Mankoff, K. D., Solgaard, A., Colgan, W., Ahlstrøm, A. P., Khan, S. A., and Fausto, R. S.: Greenland Ice Sheet solid ice discharge from 1986 through March 2020, Earth System Science Data, 12, 1367–1383, https://doi.org/10.5194/essd-12-1367-2020, 2020.

Maure, D., Kittel, C., Lambin, C., Delhasse, A., and Fettweis, X.: Spatially heterogeneous effect of climate warming on the Arctic land ice, The Cryosphere, 17, 4645–4659, https://doi.org/10.5194/tc-17-4645-2023, 2023.

Morlighem, M., Williams, C. N., Rignot, E., An, L., Arndt, J. E., Bamber, J. L., Catania, G., Chauché, N., Dowdeswell, J. A., Dorschel, B., et al.: BedMachine v3: Complete bed topography and ocean bathymetry mapping of Greenland from multibeam echo sounding combined with mass conservation, Geophysical research letters, 44, 11–051, 2017.

Mostue, I. A., Hofer, S., Storelvmo, T., and Fettweis, X.: Cloud- and ice-albedo feedbacks drive greater Greenland Ice Sheet sensitivity to warming in CMIP6 than in CMIP5, The Cryosphere, 18, 475–488, https://doi.org/10.5194/tc-18-475-2024, 2024.

Niwano, M., Aoki, T., Hashimoto, A., Matoba, S., Yamaguchi, S., Tanikawa, T., Fujita, K., Tsushima, A., Iizuka, Y., Shimada, R., and Hori, M.: NHM–SMAP: spatially and temporally high-resolution nonhydrostatic atmospheric model coupled with detailed snow process model for Greenland Ice Sheet, The Cryosphere, 12, 635–655, https://doi.org/10.5194/tc-12-635-2018, 2018.

Noël, B., van de Berg, W. J., van Wessem, J. M., van Meijgaard, E., van As, D., Lenaerts, J. T. M., Lhermitte, S., Kuipers Munneke, P., Smeets, C. J. P. P., van Ulft, L. H., van de Wal, R. S. W., and van den Broeke, M. R.: Modelling the climate and surface mass balance of polar ice sheets using RACMO2 – Part 1: Greenland (1958–2016), The Cryosphere, 12, 811–831, https://doi.org/10.5194/tc-12-811-2018, 2018.

Noël, B., Lhermitte, S., Wouters, B., and Fettweis, X.: Poleward shift of subtropical highs drives Patagonian glacier mass loss, Nature Communications, 16, 3795, 2025.

Noël, B., van de Berg, W. J., Lhermitte, S., and van den Broeke, M. R.: Rapid ablation zone expansion amplifies north Greenland mass loss, Science Advances, 5, eaaw0123, https://doi.org/10.1126/sciadv.aaw0123, 2019.

https://doi.org/10.5194/egusphere-2026-2341
Preprint. Discussion started: 2 July 2026

Ohmura, A. and Reeh, N.: New precipitation and accumulation maps for Greenland, Journal of Glaciology, 37, 140–148, https://doi.org/10.3189/S0022143000042891, 1991.

Otosaka, I. N., Shepherd, A., Ivins, E. R., Schlegel, N.-J., Amory, C., van den Broeke, M. R., Horwath, M., Joughin, I., King, M. D., Krinner, G., Nowicki, S., Payne, A. J., Rignot, E., Scambos, T., Simon, K. M., Smith, B. E., Sørensen, L. S., Velicogna, I., Whitehouse, P. L., A, G., Agosta, C., Ahlstrøm, A. P., Blazquez, A., Colgan, W., Engdahl, M. E., Fettweis, X., Forsberg, R., Gallée, H., Gardner, A., Gilbert, L., Gourmelen, N., Groh, A., Gunter, B. C., Harig, C., Helm, V., Khan, S. A., Kittel, C., Konrad, H., Langen, P. L., Lecavalier, B. S., Liang, C.-C., Loomis, B. D., McMillan, M., Melini, D., Mernild, S. H., Mottram, R., Mouginot, J., Nilsson, J., Noël, B., Pattle, M. E., Peltier, W. R., Pie, N., Roca, M., Sasgen, I., Save, H. V., Seo, K.-W., Scheuchl, B., Schrama, E. J. O., Schröder, L., Simonsen, S. B., Slater, T., Spada, G., Sutterley, T. C., Vishwakarma, B. D., van Wessem, J. M., Wiese, D., van der Wal, W., and Wouters, B.: Mass balance of the Greenland and Antarctic ice sheets from 1992 to 2020, Earth System Science Data, 15, 1597–1616, https://doi.org/10.5194/essd-15-1597-2023, 2023.

Paice, C. M., Fettweis, X., and Huybrechts, P.: Positive feedbacks drive the Greenland ice sheet evolution in millennial-length MAR–GISM simulations under a high-end warming scenario, EGUsphere, 2025, 1–45, https://doi.org/10.5194/egusphere-2025-2465, 2025.

Picard, G.: Near real-time Greenland melt extent from AMSR2 passive microwave observations at 10 km resolution (v2025), https://snow.univ-grenoble-alpes.fr/opendata/melt-AMSRU-greenland-10km.zarr, based on Picard and Fily (2006), Remote Sensing of Environment, 104(3), 325–336. Data from AMSR2 (JAXA). Accessed 2025-10-22., 2025.

Picard, G. and Fily, M.: Surface melting observations in Antarctica by microwave radiometers: Correcting 26-year time series from changes in acquisition hours, Remote Sensing of Environment, 104, 325–336, https://doi.org/https://doi.org/10.1016/j.rse.2006.05.010, 2006.

Picard, G., Leduc-Leballeur, M., Banwell, A. F., Brucker, L., and Macelloni, G.: The sensitivity of satellite microwave observations to liquid water in the Antarctic snowpack, The Cryosphere, 16, 5061–5083, https://doi.org/10.5194/tc-16-5061-2022, 2022.

Porter, C. et al.: ArcticDEM – Strips, Version 4.1, https://doi.org/10.7910/DVN/C98DVS, 2022.

Puggaard, A., Hansen, N., Mottram, R., Nagler, T., Scheiblauer, S., Simonsen, S. B., Sørensen, L. S., Wuite, J., and Solgaard, A. M.: Bias in modeled Greenland Ice Sheet melt revealed by ASCAT, The Cryosphere, 19, 2963–2981, https://doi.org/10.5194/tc-19-2963-2025, 2025.

Schaaf, C. and Wang, Z.: MCD43A3 MODIS/Terra+Aqua BRDF/Albedo Daily L3 Global - 500m V006, https://doi.org/10.5067/MODIS/MCD43A3.006, 2015.

Sellevold, R., van Kampenhout, L., Lenaerts, J. T. M., Noël, B., Lipscomb, W. H., and Vizcaino, M.: Surface mass balance downscaling through elevation classes in an Earth system model: application to the Greenland ice sheet, The Cryosphere, 13, 3193–3208, https://doi.org/10.5194/tc-13-3193-2019, 2019.

Timmermans, G.: Impact of the Presence of Surface Meltwater Lakes on the Greenland Ice Sheet Surface Mass Balance with the Help of the Regional Climate Model MAR, Master's thesis, Université de Liège, Liège, Belgique, https://matheo.uliege.be/handle/2268.2/21432, unpublished master's thesis, 2024.

Torinesi, O., Fily, M., and Genthon, C.: Variability and Trends of the Summer Melt Period of Antarctic Ice Margins since 1980 from Microwave Sensors, Journal of Climate, 16, 1047 – 1060, https://doi.org/10.1175/1520-0442(2003)016<1047:VATOTS>2.0.CO;2, 2003.

Vandecrux, B., Box, J., Mankoff, K., and Wehrlé, A.: Snow broadband albedo, specific surface area and optical grain diameter from Sentinel-3's OLCI, daily 1 km mosaics, Greenland, https://doi.org/10.22008/FK2/OIAJVO, 2021.

Vandecrux, B., Box, J. E., Ahlstrøm, A. P., Andersen, S. B., Bayou, N., Colgan, W. T., Cullen, N. J., Fausto, R. S., Haas-Artho, D., Heilig, A., Houtz, D. A., How, P., Iosifescu Enescu, I., Karlsson, N. B., Kurup Buchholz, R., Mankoff, K. D., McGrath, D., Molotch, N. P., Perren, B., Revheim, M. K., Rutishauser, A., Sampson, K., Schneebeli, M., Starkweather, S., Steffen, S., Weber, J., Wright, P. J., Zwally, H. J.,

https://doi.org/10.5194/egusphere-2026-2341
Preprint. Discussion started: 2 July 2026

and Steffen, K.: The historical Greenland Climate Network (GC-Net) curated and augmented level-1 dataset, Earth System Science Data, 15, 5467–5489, https://doi.org/10.5194/essd-15-5467-2023, 2023.

Vandecrux, B., Amory, C., Ahlstrøm, A. P., Akers, P. D., Albert, M., Alley, R. B., de Castro, M. A., Arnaud, L., Baker, I., Bales, R., Benson, C., Box, J. E., Brucker, L., Buizert, C., Chandler, D., Charalampidis, C., Cherblanc, C., Clerx, N., Colgan, W., Covi, F., Dattler, M., Denis, G., Derksen, C., Dibb, J. E., Ding, M., Dixon, D., Eisen, O., Fahrner, D., Fausto, R., Favier, V., Fernandoy, F., Freitag, J., Gerland, S., Harper, J., Hawley, R. L., Heuer, J., Hock, R., Hou, S., How, P., Humphrey, N., Hubbard, B., Iizuka, Y., Isaksson, E., Kameda, T., Karlsson, N. B., Kawakami, K., Kjær, H. A., Kreutz, K., Munneke, P. K., Lazzara, M., Lemeur, E., Lenaerts, J. T. M., Lewis, G., Lindau, F. G. L., Lindsey-Clark, J., MacFerrin, M., Machguth, H., Magand, O., Mankoff, K. D., Marquetto, L., Martinerie, P., McConnell, J. R., Medley, B., Miège, C., Miles, K. E., Miller, O., Miller, H., Montgomery, L., Morris, E., Mosley-Thompson, E., Mulvaney, R., Niwano, M., Oerter, H., Osterberg, E., Otosaka, I., Picard, G., Polashenski, C., Reijmer, C., Rennermalm, A., Rutishauser, A., Scanlan, K., Simoes, J. C., Simonsen, S. B., Smeets, P. C. J. P., Smith, A., Solgaard, A., Spencer, M., Steen-Larsen, H. C., Stevens, C. M., Sugiyama, S., Svensson, J., Tedesco, M., Thomas, E., Thompson-Munson, M., Tsutaki, S., van As, D., den Broeke, M. R. V., van Tiggelen, M., Wang, Y., Wilhelms, F., Winstrup, M., Xiao, J., and Xiao, C.: The SUMup collaborative database: Surface mass balance, subsurface temperature and density measurements from the Greenland and Antarctic ice sheets (2024 release), Arctic Data Center, https://doi.org/10.18739/A2M61BR5M, version: urn:uuid:35eb18e0-8107-4458-bc62-3cb194bb395f, 2024.

Wang, W., Zender, C. S., van As, D., and Miller, N. B.: Spatial Distribution of Melt Season Cloud Radiative Effects Over Greenland: Evaluating Satellite Observations, Reanalyses, and Model Simulations Against In Situ Measurements, Journal of Geophysical Research: Atmospheres, 124, 57–71, https://doi.org/https://doi.org/10.1029/2018JD028919, 2019.

Wu, J., Zheng, L., Chen, Z., Zhou, Q., Peng, C., Liang, Q., Li, T., Huai, B., Sun, W., Cheng, X., Law, R., and Hui, F.: Greenland supraglacial lakes albedo-depth parameterization from multi-source remote sensing: An application of lake-albedo feedback modeling, Journal of Hydrology, 662, 134 001, https://doi.org/https://doi.org/10.1016/j.jhydrol.2025.134001, 2025.

Wyard, C., Scholzen, C., Fettweis, X., Van Campenhout, J., and François, L.: Decrease in climatic conditions favouring floods in the south-east of Belgium over 1959–2010 using the regional climate model MAR, International Journal of Climatology, 37, 2782–2796, https://doi.org/https://doi.org/10.1002/joc.4879, 2017.